THE ASTROPHYSICAL JOURNAL, 414:773–792, 1993 September 10

THE EMBEDDED YOUNG STARS IN THE TAURUS-AURIGA MOLECULAR CLOUD. II. MODELS FOR SCATTERED LIGHT IMAGES

SCOTT J. KENYON,[1] BARBARA A. WHITNEY, MERCEDES GOMEZ,[1] AND LEE HARTMANN
Harvard-Smithsonian Center for Astrophysics, 60 Garden Street, Cambridge, MA 02138
Received 1993 February 16; accepted 1993 March 16

ABSTRACT

We describe near-infrared imaging observations of embedded young stars in the Taurus-Auriga molecular cloud. We find a large range in $J-K$ and $H-K$ colors for these class I sources. The bluest objects have colors similar to the reddest T Tauri stars in the cloud; redder objects lie slightly above the reddening line for standard ISM dust and have apparent K extinctions of up to 5 mag. Most of these sources also show extended near-IR emission on scales of 10″–20″, which corresponds to linear sizes of 1500–3000 AU. The near-IR colors and nebular morphologies for this sample and the magnitude of linear polarization in several sources suggest scattered light produces most of the near-IR emission in these objects.

We adopt the Terebey, Shu, and Cassen solution for an infalling, rotating protostellar cloud and use a two-dimensional Monte Carlo radiative transfer code to model the near-IR colors and images for the embedded sample. Our results suggest mass infall rates that agree with predictions for cold clouds ($T \sim 10$–20 K) and are generally consistent with rates estimated from radiative equilibrium models in a previous paper (e.g., $\dot{M} \sim 2$–$10 \times 10^{-6}\ M_\odot\ \mathrm{yr}^{-1}$). For reasonable dust grain parameters, the range of colors and extinctions require flattened density distributions with polar cavities evacuated by bipolar outflows. These results support the idea that infall and outflow occur simultaneously in deeply embedded, bipolar outflow sources. The data also indicate fairly large centrifugal radii, $R_c \sim 100$ AU, and large inclinations to the rotational axis, $i \sim 60°$–$90°$, for a typical source. Our centrifugal radius estimates agree with the disk radii inferred for many T Tauri stars in the Taurus-Auriga cloud. Better maps of polarization and molecular outflows in these objects can test our inclination estimates.

Subject headings: infrared: stars — radiative transfer — stars: formation — stars: pre–main-sequence

1. INTRODUCTION

The standard model for the formation of a single, low-mass star begins with the collapse of a slowly rotating, nearly isothermal cloud of gas and dust. During the early stages of this process, material close to the center of the cloud condenses into a starlike core while more distant gas in the equatorial plane forms a circumstellar disk. As the collapse proceeds, low angular momentum material continues to fall into or very close to the central star; higher angular momentum material lands in the disk. At some point, a wind from the star-disk system—whose physical origin remains uncertain—clears gas and dust away from the rotational axis to produce a bipolar molecular outflow. All of the cloud eventually falls into the star-disk system or gets swept away by the wind (or both) to reveal a pre–main-sequence star surrounded by a large ($R \sim 100$ AU) circumstellar disk. Shu, Adams, & Lizano (1987; see also Terebey, Shu, & Cassen 1984, hereafter TSC; Adams & Shu 1986) describe the physics of the collapse process in more detail, while Königl (1991), Pudritz & Norman (1986), and Shu et al. (1988) have explored possible mechanisms to produce bipolar outflows.

Recent observations of nearby molecular clouds support this general picture of star formation. Several surveys using data from the *Infrared Astronomical Satellite* (*IRAS*) have identified a population of embedded sources (also known as class I sources and "protostars") that emit most of their luminosity at wavelengths of 10–200 μm (e.g., Beichman et al. 1986; Myers et al. 1987; Wilking, Lada, & Young 1989). These objects usually appear closely associated with extended optical and near-infrared (near-IR) emission, eject molecular gas at modest velocities, and lie close to the centers of dense cloud cores (e.g., Tamura et al. 1991; Terebey, Vogel, & Myers 1989; Benson & Myers 1989). They are also among the very youngest stellar sources in nearby molecular clouds, with estimated ages of $\sim 10^5$ yr based on source statistics (e.g., Myers et al. 1987; Wilking et al. 1989). Detailed radiative transfer calculations for several embedded sources generally verify the age estimates and confirm the sharp density rise close to the source predicted by the standard model (see Myers et al. 1987; Adams, Lada, & Shu 1987, hereafter ALS; Butner et al. 1991).

The surveys for embedded sources in the Taurus-Auriga cloud now seem fairly complete down to a bolometric luminosity of $L \sim 0.1$–$0.2\ L_\odot$ (see Kenyon et al. 1990; Beichman, Boulanger, & Moshir 1992, and references therein), so it seems appropriate to model a large population of embedded sources in a single molecular cloud. In an earlier paper (Kenyon, Calvet, & Hartmann 1993, hereafter Paper I), we calculated spherically averaged radiative equilibrium models of infalling, dusty envelopes for the Taurus-Auriga sample and estimated infall rates, centrifugal radii, and inclinations from fits to their spectral energy distributions. We found that the observed far-IR peaks indicate infall rates close to those predicted for thermally supported cloud cores with temperatures of ~ 10–20 K (e.g., an infall rate of $\sim 4 \times 10^{-6}\ M_\odot\ \mathrm{yr}^{-1}$). The observed spectral energy distributions appear much broader than expected for spherically symmetric infall and generally agree with models using TSC's rotationally flattened density distribution. We estimate centrifugal radii of ~ 70 AU for many

[1] Visiting Astronomer, Kitt Peak National Observatory.

objects, which is reasonably consistent with the characteristic sizes of circumstellar disks around T Tauri stars (Adams, Emerson, & Fuller 1990; Beckwith et al. 1990).

In spite of our success in reproducing the spectral energy distributions of the Taurus-Auriga sources for reasonable infall rates and centrifugal radii, the radiative transfer models have several deficiencies. First, our centrifugal radius estimates are uncertain, because we employed a spherically averaged density distribution—instead of the exact axisymmetric solution—to solve the radiative transfer equation. More importantly, our models failed to account for the large amount of 1–3 μm emission observed in nearly all embedded sources, and we were forced to adopt relatively low source inclinations, $i \lesssim 30°$, to produce enough 3–5 μm radiation in many sources. The ubiquitous nature of *extended* near-IR emission in most embedded sources argues that scattering dominates the 1–3 μm light in these objects (e.g., Heyer et al. 1990; Tamura et al. 1991). Although we explicitly included isotropic scattering in Paper I's calculations, we could not properly model scattering for the TSC density distribution. We also could not consider the possibility that a molecular outflow produces a bipolar hole in the density distribution. Most embedded sources with extended reflection nebulae also seem associated with high-velocity molecular gas (see Paper I and below), so bipolar holes probably occur in at least some objects.

This paper extends our study of the Taurus-Auriga embedded sources with a more detailed investigation of their near-IR properties. We begin with broad-band images to derive near-IR colors and to estimate the relative importance of scattering and extinction. We then build upon Paper I's radiative transfer models with a two-dimensional Monte Carlo code to try to reproduce these observations for physically plausible input parameters. For infall rates consistent with the far-IR spectral energy distributions, we find that scattering of near-IR radiation by dust in the envelope can account for the near-IR colors and image morphology only if the envelopes have bipolar holes (i.e., evacuated cavities along the rotational axis of the cloud). Models *without* large cavities can produce some of the observed colors but very few of the observed images. This result argues strongly that mass loss begins very early in the infall phase and carves out bipolar cavities in the envelope through which radiation from the central star escapes by scattering.

We describe our observations in § 2, compare them to model predictions in § 3, and conclude with a brief discussion in § 4.

2. OBSERVATIONS

2.1. *Sample Selection*

We define embedded sources as pre–main-sequence stars whose ratio of *IRAS* to bolometric luminosity is $L_{IRAS}/L_{bol} \gtrsim 0.8$ (Paper I). This definition includes all class I objects with steeply rising spectral energy distributions from 2 μm to 25–100 μm (ALS; see also Myers et al. 1987; Kenyon et al. 1990) but excludes optically visible TTS with large *IRAS* luminosities (e.g., DG Tau; see Adams et al. 1990). In Paper I, we added several other pre–main-sequence objects—HK Tau and Haro 6–13—to this sample, because their spectral energy distributions suggest a close similarity to GV Tau (which contains a T Tauri star and an embedded source; see Leinert & Haas 1989). However, we exclude these systems from this study, because near-IR observations of their individual component stars do not exist. Table 1 lists our sample of objects and summarizes other relevant information including mean near-IR colors, *IRAS* and bolometric luminosities from Paper I, the polarization at *K*, and notes on the presence of extended near-IR emission (ext) and high-velocity molecular gas (hvg).

2.2. *Near-Infrared Imaging Observations*

We acquired near-infrared images for most of the embedded sample with the Simultaneous Quad Infrared Imaging Device (SQIID) mounted at the Kitt Peak National Observatory

TABLE 1

PROPERTIES OF TAURUS-AURIGA EMBEDDED SOURCES

IRAS Name	Other ID	$J-K$	$H-K$	L_{IRAS}	L_{bol}	$p(K)$	ext	hvg
04016+2610	L1489 IRS	4.0	2.1	3.10	3.70	10%–70%	yes	yes
04108+2803B		4.9	1.9	0.61	0.64		no	no
04166+2706			2.4	0.29	0.31		no	?
04169+2702		4.9	2.6	0.72	0.74		yes	yes
04181+2655		4.9	2.2	0.36	0.36		maybe	?
04181+2654B		7.3	2.8	0.45	0.25		yes	?
04181+2654A		5.2	2.1	0.45	0.26		maybe	?
04239+2436		5.0	2.6	1.10	1.20		yes	yes
04248+2612	HH31 IRS2	2.0	0.8	0.32	0.35		yes	yes
04263+2426	GV Tau B		1.7	5.90	6.30	2–4	yes	?
04264+2433		2.5	0.9	0.34	0.37		yes	?
04287+1801	L1551 IRS5	3.8	1.7	21.1	21.50	24	yes	yes
04295+2251	L1536 IRS	4.0	1.5	0.34	0.43		no	no
04302+2247		3.1	1.3	0.31	0.33		yes	yes
04325+2402			2.0	0.68	0.70		yes	yes
04361+2547	TMR-1	5.4	2.4	2.70	2.80		yes	yes
04365+2535		6.5	2.9	2.10	2.20		yes	yes
04368+2557	L1527 IRS	2.8	1.6	1.30	2.10		yes	yes
04381+2540		4.2	2.2	0.64	0.65		yes	yes
04489+3042		3.6	1.3	0.25	0.29		no	?

NOTES.—Data are from Heyer et al. (1987; molecular outflows); Heyer et al. (1990; near-IR images; polarimetry); Kenyon et al. (1993; near-IR photometry; luminosities); Moriarty-Schieven et al. (1992; molecular outflows); Myers et al. (1988; molecular outflows); Nagata et al. (1983; polarimetry); Tamura & Sato (1989; polarimetry); Tamura et al. (1991; near-IR images); Terebey et al. (1989; molecular outflows). Luminosities are in $L_\odot$.

TABLE 2

SQIID PHOTOMETRY OF TAURUS-AURIGA EMBEDDED SOURCES

		8″ APERTURE			13″ APERTURE			26″ APERTURE		
IRAS NAME	JD	K	$J-K$	$H-K$	K	$J-K$	$H-K$	K	$J-K$	$H-K$
04016+2610	8560.7	9.54	4.33	2.42	9.35	4.04	2.22	9.23	3.89	2.14
04108+2803A	8560.8	10.38	3.21	1.24	10.34	3.19	1.23	10.34	3.17	1.23
04108+2803B	8560.8	11.64	4.95	1.91	11.56	4.90	1.86	11.48	4.87	1.85
04166+2706	8561.7	11.67	>4.40	2.54	11.54	>4.40	2.47	11.49	>4.40	2.43
04169+2702	8561.7	11.43	>5.00	2.77	11.24	4.90	2.64	10.99	4.80	2.59
04181+2655	8562.7	10.76	4.95	2.16	10.70	4.92	2.17	10.63	4.91	2.17
04181+2654B	8562.7	10.88	7.45	2.85	10.80	7.30	2.83	10.66	7.21	2.93
04181+2654A	8562.7	10.44	5.26	2.10	10.37	5.23	2.07	10.30	5.24	2.12
04239+2436	8564.8	10.72	4.80	2.48	10.69	4.74	2.41	10.62	4.79	2.40
04248+2612	8562.7	10.67	2.03	0.80	10.40	1.98	0.75	10.18	1.94	0.75
04295+2251	8564.9	9.63	3.99	1.64	9.59	3.91	1.62	9.57	3.90	1.61
04325+2402	8562.7	11.27	>5.50	2.05	10.96	>5.50	1.99	10.64	>5.50	1.86
04361+2547	8565.0	10.56	5.65	2.22	10.44	5.72	2.21	10.28	5.80	2.27
04365+2535	8564.8	10.45	6.66	2.85	10.31	6.80	2.68	10.23	6.88	2.66
04368+2557	8562.9							11.10	2.80	1.60
04381+2540	8565.0	12.11	>4.00	2.41	11.96	>4.00	2.43	11.92	>4.00	2.41
04489+3042	8564.9	10.13	3.89	1.66	10.10	3.67	1.65	10.06	3.67	1.64

NOTES.—We include photometry of 04108+2803A for completeness, even though it does not meet our criterion for a class I object.

Kenyon et al. 1990 incorrectly identified 04181+2655 as 04181+2654; their Table II also contains a misprint: $H-K$ should be 2.28 (not 1.28). This group contains three embedded sources; our measured offsets from 04181+2654A are $(\delta\alpha, \delta\delta) = (-14''.2, +26''.4)$ for 04181+2655B and $(-46''.0, +67''.3)$ for 04181+2654.

Photometry for 04368+2557 is very uncertain due to its large size (40″ × 20″) and low surface brightness (K = 16–17 per pixel). Tamura et al. 1990 estimated K = 13 for this object from IRIM data. The Julian Date is 2440000 + JD listed above.

(KPNO) 1.3 m telescope during 1991 October 30 to November 3 (Ellis et al. 1992). SQIID records JHKL images of 5′ × 5′ fields on four 256 × 256 platinum silicide arrays. We took five 120 s exposures for each object and offset the telescope by 40″ in both right ascension and declination after each integration. Final object frames were produced by dividing the raw frames with an appropriate flat field and then subtracting a flattened sky frame. To construct a flat-field image for each filter, we subtracted an average 120 s dark frame from all of our 120 s object frames, median filtered each set of five exposures, and then averaged this result. The sky frame is the median filtered image of the five object images obtained with each filter.

We used the NOAO IRAF routine PHOT to extract photometry through 8″, 13″, and 26″ apertures for each embedded source and reduced these data to the Elias et al. (1982) system using standard techniques. Table 2 lists our JHK results; we detected only 04016+2610 at L and thus did not calibrate these images. Repeat measurements of several embedded objects and various point sources with K = 6–11 suggest the internal accuracy of the SQIID magnitude scale is ±0.03 mag. Our comparisons with previous observations of red field stars and several pre–main-sequence objects indicate our magnitudes have a small zero point offset at K and color terms for $H-K$ and $J-K$ with respect to the standard CIT magnitude system. These corrections are small—~5% for $J-K$ and $H-K$—and not statistically significant given our modest number of standard star observations (six to seven measurements of ~20 Elias et al. 1982 and other red standards). We need a larger ensemble of standard star observations to verify the color terms and therefore ignore them in this paper.

We acquired additional near-IR images of several embedded sources during 1990 October 11–15 with the IR imager (IRIM) mounted on the 1.3 m telescope at KPNO (Fowler et al. 1987). The IRIM records a 1′ × 1′ field on a 62 × 58 InSb array through standard IR interference filters. We took 15 frames at *JHK*—five per filter—and displaced the telescope by 8″ in both right ascension and declination after each integration. A median-filtered image constructed from each set of five images served as a sky frame for an object, while the sum of all long exposure sky frames served as our flat field. Once each frame had been flattened and sky-subtracted, we used PHOT to extract photometry through our three apertures and reduced these results to the Elias et al. (1982) system. The internal precision of the imager photometry listed in Table 3 appears

TABLE 3

IRIM PHOTOMETRY OF TAURUS-AURIGA EMBEDDED SOURCES

		8″ APERTURE			13″ APERTURE			26″ APERTURE		
IRAS NAME	JD	K	$J-K$	$H-K$	K	$J-K$	$H-K$	K	$J-K$	$H-K$
04108+2803A	8176.782	10.38	3.27	1.25	10.36	3.29	1.23	10.35	3.30	1.22
04108+2803B	8176.782	10.60	5.55	2.48	10.61	5.56	2.49	10.60	5.56	2.47
04181+2655	8175.849	10.74		2.25	10.70		2.23	10.67		2.19
04181+2654B	8175.844	10.90		2.82	10.84		2.82	10.74		2.78
04248+2612	8178.981	10.68	2.14	0.80	10.43	2.11	0.78	10.11	2.08	0.75

NOTE.—We include photometry of 04108+2803A for completeness, even though it does not meet our criterion for a class I object. The Julian Date is 2440000 + JD listed above.

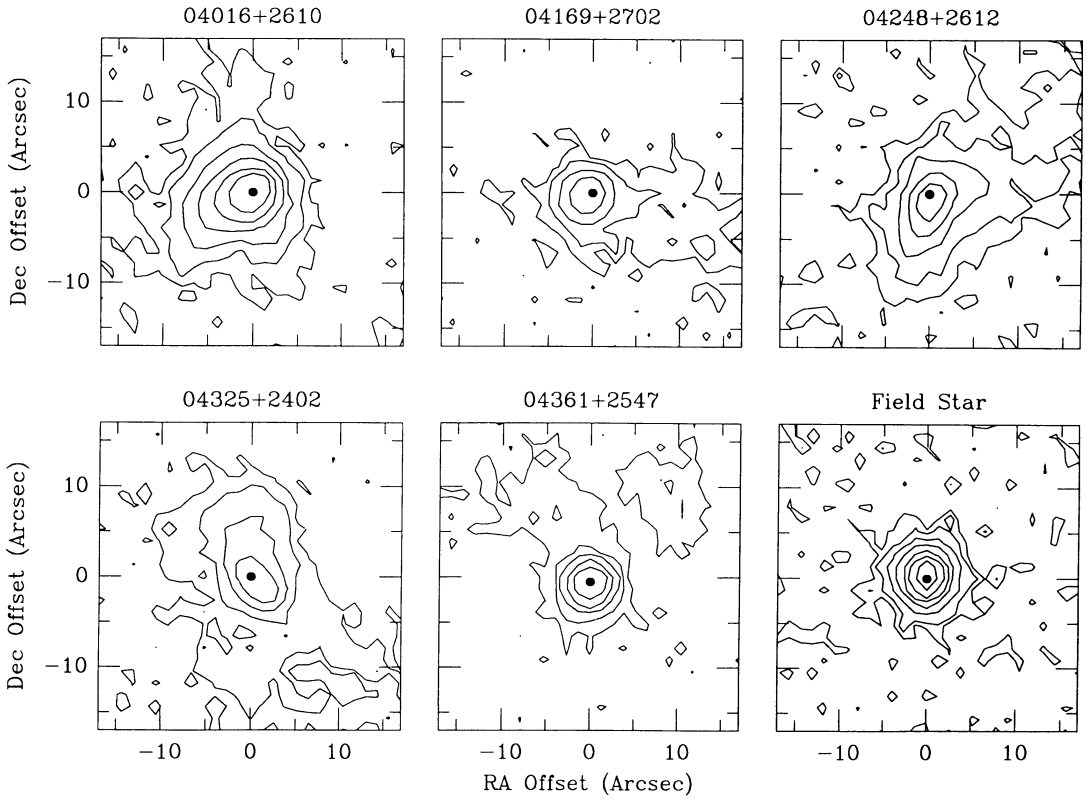

FIG. 1.—Contour maps for K images of five embedded *IRAS* sources and a field star. The contours are spaced at intervals of 1 mag from peak intensity, which is indicated by a filled circle in each panel.

comparable to that of our SQIID data—$\pm 3\%$ at JHK—based on repeat measurements of several sources.

2.3. *Results*

Figures 1–4 show contour maps for most of the class I sources along with a point source for comparison. We find extended near-IR emission surrounding nearly every object in our sample. This emission appears very weakly in some sources—such as 04181+2655 and 04166+2706—but only 04108+2803B, 04295+2251, and 04489+3042 show no trace of nebulosity on our SQIID images. The contour maps display a wider range of morphologies; several embedded sources appear V-shaped (04016+2610 and 04248+2512), while others look rectangular (04325+2402, 04169+2702, and 04361+2547) or amorphous (04368+2557). Tamura et al. (1991) reported similar results for K images of a smaller sample of embedded sources. With the exception of 04368+2557, all of the objects in our sample possess a strong central point source at K. We took great care to register stellar sources on our JHK images of 04368+2557, so the apparent displacement of its nebulosity as a function of wavelength (Fig. 4) appears to be real. Confirmation of this result awaits deeper near-IR images of this object.

We detected extended emission at J and H in many sources, so our data provide useful information on the color indices of the central point source and its surrounding nebulosity. The nebulosity of a few embedded sources—04016+2610, 04169+2706, 04248+2612, and 04325+2402—appears *bluer* than the central starlike core, while two other embedded sources—04361+2547 and 04365+2535—possess nebulae that appear *redder* than the star (see also Heyer et al. 1990; Terebey et al. 1990). For the remaining sources, the nebulae either have the same colors as the central star or are too faint to measure accurately.

The left panel of Figure 5 shows a $J-K$, $H-K$ color-color diagram for optically visible pre–main-sequence stars (TTS; *small filled circles*) and our embedded sample (*large open circles*) in the Taurus-Auriga cloud. Roughly half of the embedded objects display near-IR colors comparable to the reddest TTS, while the rest appear much redder than any TTS. These data fall along a locus with a slightly larger slope than the reddening line for standard galactic dust. If we assume that the central young star within an embedded object has intrinsic colors similar to those of an unreddened TTS, then the observed colors roughly correspond to line-of-sight extinctions ranging from $A_V \sim 5$ mag to $A_V \sim 25$–30 mag (Table 4). These extinctions imply molecular hydrogen column densities of $N(H_2) \sim 1$–6×10^{21} cm^{-2} for a standard gas-to-dust ratio (e.g., Savage & Mathis 1979; Mathis 1990).

To provide an independent estimate for the K extinction, we derive an "intrinsic" K magnitude of the underlying pre–main-sequence star from the bolometric luminosity. We assume that the embedded star (1) has a bolometric luminosity equal to the integrated luminosity from ~ 1 μm to 100–1000 μm (Paper I presents spectral energy distributions and the observed wavelength range for each embedded source), (2) lies on a 10^5 yr isochrone (Stahler 1983, 1988; Mazzitelli 1989), and (3) has an intrinsic spectral energy distribution similar to that of a typical T Tauri star. With these assumptions, we convert the bolometric luminosities from Table 1 into intrinsic J-magnitudes (see Kenyon & Hartmann 1990; Gomez et al. 1992) and then apply an average $J-K$ color ($\langle J-K \rangle = 1.5 \pm 0.7$ for TTS;

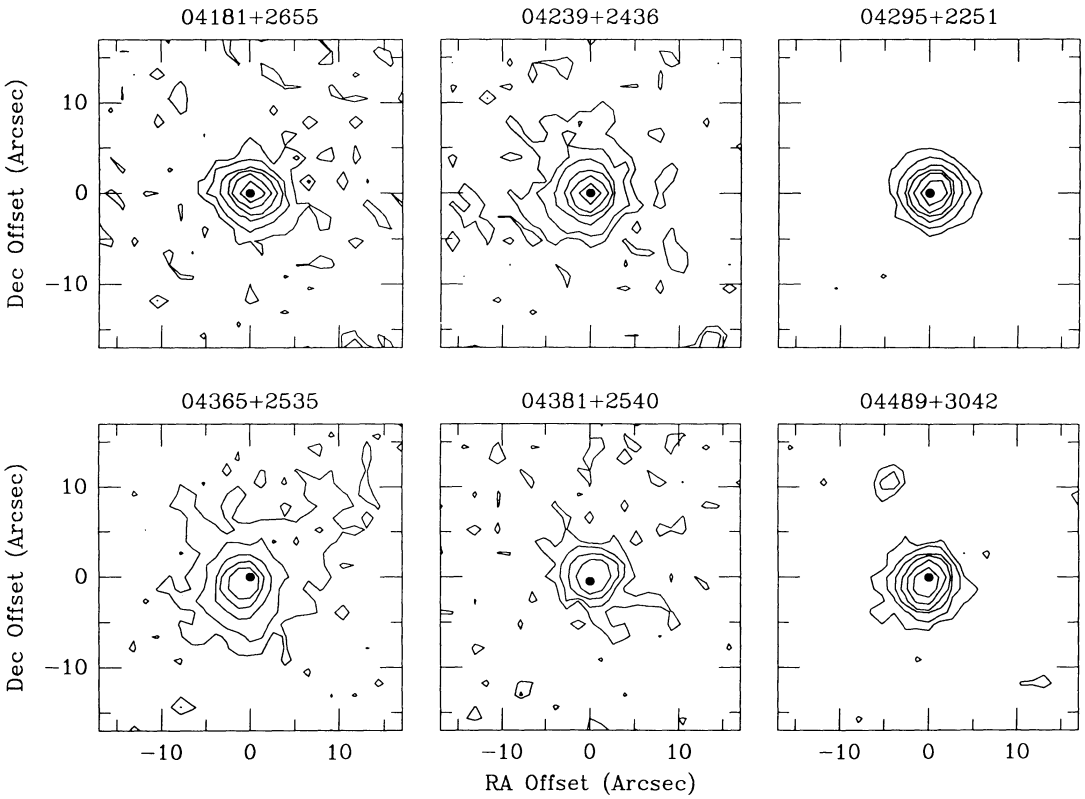

FIG. 2.—Contour maps for *K* images of six embedded *IRAS* sources

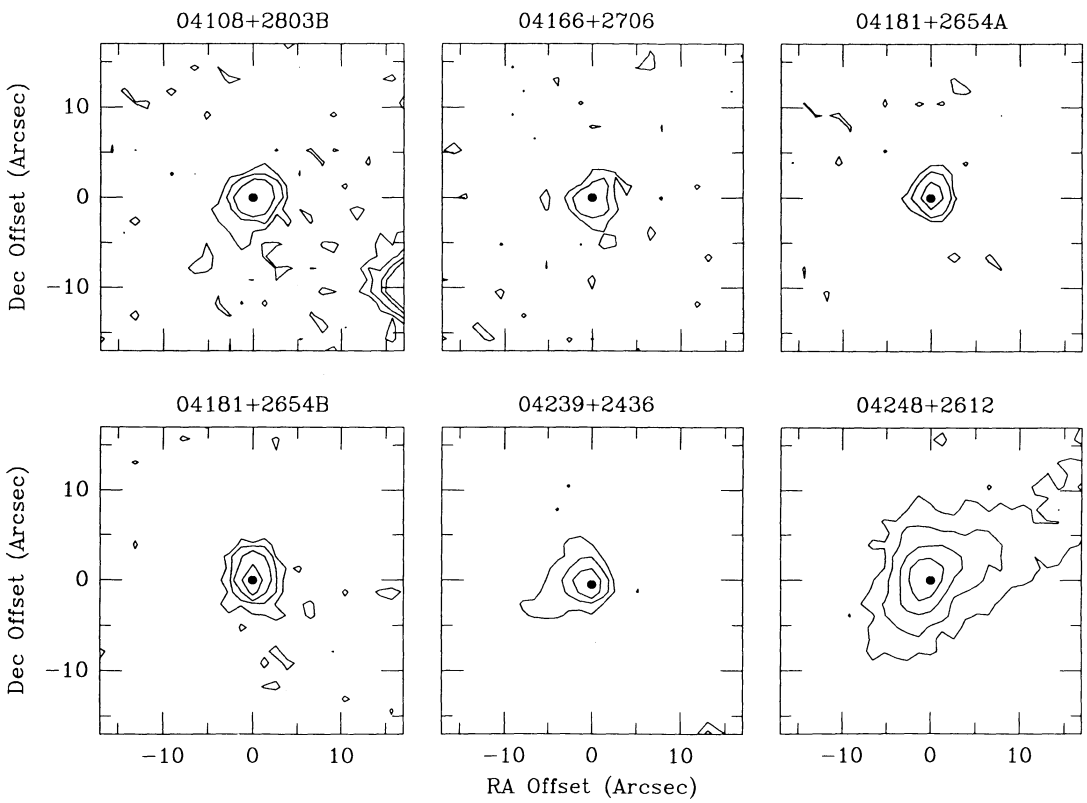

FIG. 3.—Contour maps for *H* images of six embedded *IRAS* sources

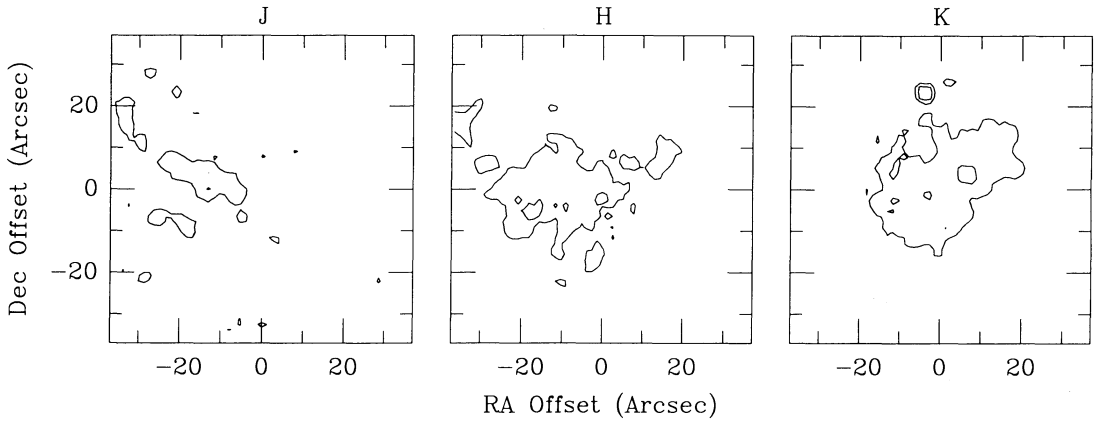

FIG. 4.—*JHK* contour maps for the embedded *IRAS* source 04368+2557. The gradual spatial shift in emission as a function of wavelength seems real, as described in the text.

Kenyon & Hartmann 1993) to correct J_0 into K_0. We estimate the uncertainty in our derived K_0 to be ± 1 mag based on dispersions in the relations between bolometric correction, $J-K$, and spectral type (ST). Our adopted 10^5 yr age reasonably accounts for the relative numbers and energy distributions of these sources (Myers et al 1987; Kenyon et al. 1990; Paper I).

Table 4 lists our estimated K_0 for the embedded sources, while the right panel of Figure 5 plots the difference between the observed and "intrinsic" K-magnitudes, $K-K_0$, as a function of observed $H-K$. These data imply apparent line-of-sight extinctions, $A_K \sim 1$–5 mag, that agree fairly well with those estimated from Figure 2 and that are a factor of 2–3 less than those estimated from the observed 800 μm fluxes (Barsony & Kenyon 1992).

ALS proposed scattered light as the dominant source of near-IR emission in class I sources based on fits to spectral energy distributions (see also Paper I), while Barsony & Kenyon (1992) reached the same conclusion to reconcile the large difference between near-IR and submillimeter dust column densities. The Heyer et al. (1990) polarization map of 04016+2610 (with p vectors of $\sim$20%–60% at K) supports this argument for at least one embedded source, because scattering can produce a diffuse, polarized image when the central star is completely obscured and the geometry is not spherically symmetric (Bastien & Ménard 1988, 1990; Whitney & Hartmann 1992, 1993, and references therein). The near-IR light of L1551 IRS5 and GV Tau B is also highly polarized (Nagata, Sato, & Kobayashi 1983; Tamura & Sato 1989), while 04248+2612 and several other embedded sources show weak 1–3 μm peaks in their spectral energy distributions (Paper I). These observations point to scattering as the main source of near-IR light; unfortunately, the spectral energy distributions of most embedded sources do not display as clearly the near-IR peaks, and very few have measured polarizations.

A nonstandard extinction law within the molecular cloud core seems the best alternative to the scattered light hypothesis. Pendleton, Tielens, & Werner (1990) suggested that grains in a dense molecular cloud might grow to larger sizes than those in the interstellar medium, because the higher local parti-

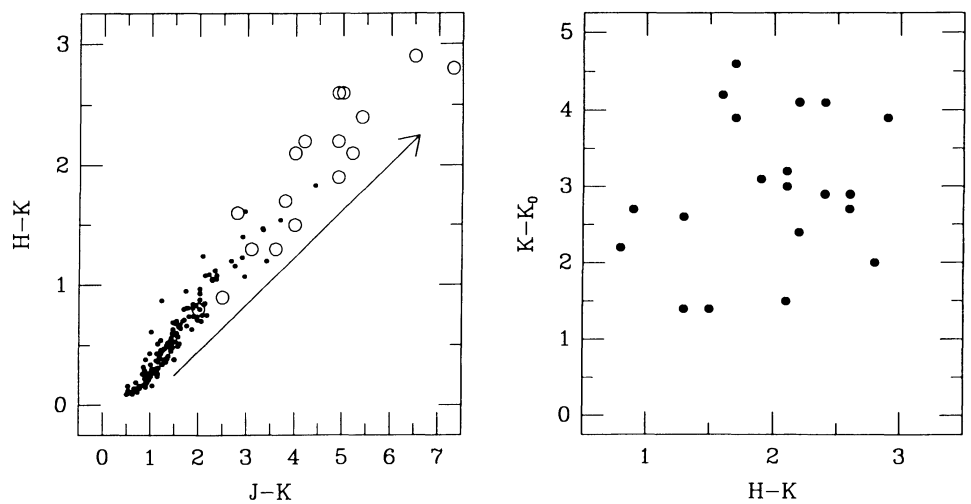

FIG. 5.—*Left panel*: color-color diagram for pre–main-sequence stars in the Taurus-Auriga dark cloud. The small filled circles plot $J-K$ and $H-K$ colors for optically visible T Tauri stars (classical and weak emission stars; Kenyon & Hartmann 1993), while large open circles plot colors for the embedded sources listed in Table 1. The long arrow corresponds to a reddening line for $A_V = 25$ mag. *Right panel*: color-extinction diagram for Taurus-Auriga embedded sources. The quantity $K-K_0$ estimates the apparent line-of-sight extinction to the central stellar source, as described in the text.

TABLE 4

ESTIMATED PROPERTIES OF EMBEDDED SOURCES

IRAS Name	K	ST	J_0	K_0	$K-K_0$	$\dot{M}$	R_c	i
04016+2610	9.5	K5	7.8	6.3	3.2	4–7	50–200	60–90
04108+2803B	11.0	M4	9.4	7.9	3.1	4–7	50–200	60–90
04166+2706	11.7	M5	10.1	8.6	3.1	5–10	100–300	60–90
04169+2702	11.4	M3	9.3	8.1	3.4	7–10	200–300	60–90
04181+2655	10.8	M5	9.8	8.3	2.5	5–10	50–300	30–60
04181+2654B	10.9	M5	10.3	8.8	2.1	4–7	50–200	30–60
04181+2654A	10.4	M5	10.3	8.8	1.6	5–10	100–300	30–60
04239+2436	10.1	M2	8.9	7.4	2.7	5–10	200–300	60–90
04248+2612	10.7	M5	10.0	8.5	2.2	2–4	50–200	60–90
04263+2426	9.8	K3	7.4	5.9	3.9	4–7	50–200	60–90
04264+2433	11.1	M5	9.9	8.4	2.7	2–4	50–200	60–90
04287+1801	9.3	K0	6.2	4.7	4.6	4–7	50–200	60–90
04295+2251	9.6	M5	9.7	8.2	1.4	1–5	10–1000	30–90
04302+2247	11.1	M5	10.0	8.5	2.6	2–5	50–200	60–90
04325+2402	11.3	M3	9.4	7.9	3.4	4–6	50–200	60–90
04361+2547	10.6	M0	8.0	6.5	4.1	7–10	300–1000	60–90
04365+2535	10.5	M1	8.3	6.8	3.7	4–7	50–200	60–90
04368+2557	11.1	M1	8.4	6.9	4.2	1–4	10–200	60–90
04381+2540	12.0	M4	9.4	7.9	4.1	4–7	50–200	60–90
04489+3042	10.1	M5	10.2	8.7	1.4	1–5	10–1000	30–90

NOTES.—The mass infall rates estimated above are measured in units of $10^{-6}\,M_\odot\ \mathrm{yr}^{-1}$; the centrifugal radii are measured in AU; the inclination is measured in degrees from the rotational axis.

The two reddest sources are fit with no hole, 04181+2654B and 04365+2535.

cle densities and better shielding from UV radiation favor high accretion rates of ices onto carbon and silicate grains. These grains produce both a small ratio of near-IR to submillimeter extinction and a relatively gray extinction curve at optical and near-IR wavelengths compared to the standard grain size distribution. Thus, large grains might account for the observed ratio of near-IR to submillimeter light among embedded sources. These grains should also cause surrounding nebulosities to have redder near-IR colors than "standard" grains, because their albedo is nearly constant at these wavelengths. The observations of the embedded sources show a wide range of $H-K$ and $J-K$ colors that can test scattering models for different grain species in detail, so we now consider two-dimensional radiative transfer calculations for the standard infall geometry.

3. SCATTERING MODELS

3.1. *Envelope Structure and Calculational Procedure*

TSC (see also Ulrich 1976; Cassen & Moosman 1981) present a complete description of our adopted model for an infalling protostellar cloud. The cloud initially rotates as a solid body with angular velocity, Ω, and has the density distribution, $\rho(r)$, of a singular isothermal sphere, $\rho \propto r^{-2}$. Material falls in toward the center of the cloud at a constant rate, $\dot{M} \propto a^3$, where a is the sound speed. At any time t, gas and dust inside a radius, $r_s = at$, flow toward the central object at the free-fall velocity, and the density structure approaches, $\rho \propto r^{-3/2}$. The cloud rests in its initial structure outside this radius. Angular momentum affects the collapse near the centrifugal radius, $R_c \equiv G^3M^3\Omega^2/16a^3$, which grows with time as t^3 (TSC; Adams & Shu 1986). Material lying along the cloud's rotational axis falls into the central object, while gas with large angular momentum lands in a circumstellar disk (Ulrich 1976; Cassen & Moosman 1981).

Whitney & Hartmann (1992, 1993) describe the Monte Carlo radiative transfer code we use to calculate near-IR images for embedded sources. We assume a central source that illuminates a circumstellar disk and infalling envelope; some type of outflow carves out a bipolar cavity within the envelope. The disk and envelope scatter photons from the central source; we ignore thermal emission from this material, because these photons are emitted at wavelengths exceeding 10 μm (Paper I). The Monte Carlo code follows the trajectory and polarization of each photon through multiple scatterings off the disk + envelope and collects the escaping photons into grids to construct images and polarization maps at each of 11 angle bins centered at $\mu \equiv \cos i = 0.0, 0.1, 0.2, \ldots, 0.9, 0.975$.

The appearance of model near-IR images depends on the adopted envelope structure and the physical properties of the dust grains. We employ the Henyey-Greenstein function to approximate the scattering and White's parameters for polarization (see Whitney & Hartmann 1992, 1993). The scattering properties of the dust are then set by the opacity, κ; the scattering albedo, ω; the maximum polarization for 90° scattering, $p_{\max}$; and the scattering asymmetry parameter, g. The albedo is the ratio of scattering to total opacity. The asymmetry parameter defines the forward-throwing properties of the dust and ranges from $g = 0$ (isotropic scattering) to $g = 1$ (scattering in the incident, or forward, direction). The polarization of light scattered off interstellar dust is similar to that predicted for Rayleigh scattering, except that the magnitude of polarization is smaller for interstellar dust (White 1979). The variable $p_{\max}$ sets the maximum polarization for each wavelength. We adopt grain parameters for two different grain size distributions. The Mathis, Rumpl, & Nordsieck (1977, hereafter MRN) distribution successfully accounts for the diffuse ISM reddening law from ultraviolet to near-IR wavelengths; we will adopt MRN grains as our "standard" grain model with optical constants from Draine & Lee (1984). Pendleton, Tielens, & Werner (1990, hereafter PTW) argued that larger grains might be more appropriate for the denser conditions inside molecular clouds, so we consider these larger grains for comparison. Table 5 lists the characteristics of the two grain size distributions. MRN

TABLE 5

GRAIN PROPERTIES

Grain Model	λ (μm)	κ (cm^2 gm^{-1})	ω	g	p_{max}
MRN (J)	1.25	65	0.42	0.16	0.75
MRN (H)	1.65	38	0.33	0.06	0.87
MRN (K)	2.20	20	0.21	0.03	0.93
PTW (J)	1.25	115	0.77	0.53	0.20
PTW (H)	1.65	98	0.76	0.45	0.30
PTW (K)	2.20	75	0.72	0.36	0.42

grains scatter isotropically and have low albedos, a steep opacity function and high polarization; the PTW grains scatter more in the forward direction and have high albedos, a flatter opacity law, and low polarization.

The physical variables defining the envelope structure include the central mass, M_*; the mass infall rate, $\dot{M}$; the centrifugal radius, R_c; and the shape of the hole created by a bipolar outflow. As in Whitney & Hartmann (1993), we assume dusty material falls toward a central 0.5 $M_\odot$ object throughout a cloud with maximum radius $r_{max} = 1.1 \times 10^4$ AU, which is the radius enclosing 1 $M_\odot$ in a spherical, isothermal, hydrostatic cloud having a sound speed of 0.2 km s^{-1} (Shu 1977). If $\dot{M}$ is constant throughout the cloud, the density distribution as a function of radius and inclination angle ($\mu = \cos i$) is

$$\rho = \frac{\dot{M}}{4\pi}\left(\frac{GM_*}{R_c^3}\right)^{-1/2}\left(\frac{r}{R_c}\right)^{-3/2}\left(1+\frac{\mu}{\mu_0}\right)^{-1/2}\left(\frac{\mu}{\mu_0}+\frac{2\mu_0^2 R_c}{r}\right)^{-1}, \quad (1)$$

where μ_0 is the inclination angle of an orbit as $r \rightarrow \infty$ and the centrifugal radius, R_c, is:

$$R_c \approx 800\left[\left(\frac{\Omega}{1 \text{ km s}^{-1} \text{ pc}^{-1}}\right)\left(\frac{r_{max}}{1.1 \times 10^4 \text{ AU}}\right)^2\right]^2 \times \left(\frac{M_*}{0.5\ M_\odot}\right)^{-1} \text{AU} . \quad (2)$$

At large radii, $r \gg R_c$, the density distribution decreases as $\rho \propto r^{-3/2}$ and resembles a spherical cloud; the density distribution becomes flattened close to $r \sim R_c$ and then approaches $\rho \propto r^{-1/2}$ for $r \ll R_c$ because material falls into the disk instead of the central star (TSC). Figure 1 of Whitney & Hartmann (1993) shows the density distribution for this cloud.

We introduce a polar hole in the envelope to model the consequences of bipolar outflows and adopt a completely evacuated cavity for simplicity. For most models, we assume that the shape of the hole follows the streamline of an infalling particle (Whitney & Hartmann 1993); we also consider a more curved streamline, $z \propto \varpi^{1.5}$ (where ϖ is the cylindrical radius), to see how model images depend on the hole shape.

For a given opening angle of the hole, θ_H, and viewing angle, i, the optical depth through the envelope varies as $\tau \propto \kappa \dot{M} M_*^{-1/2} R_c^{-1/2}$ as long as R_c remains small compared to r_{max} (Whitney & Hartmann 1993). The infall rate depends only on the sound speed in the cloud; $\dot{M} \sim 2 \times 10^{-6}\ M_\odot$ yr^{-1} for $a = 0.2$ km s^{-1} in the Taurus-Auriga cloud (ALS; Myers et al. 1987). Significant nonthermal motions within the cloud could increase the infall rate above this value, so we consider a range in infall rates: $\dot{M} = 1$–$20 \times 10^{-6}\ M_\odot$ yr^{-1}. Goodman et al. (1993) report velocity gradients of 0.3–4 km s^{-1} pc^{-1} in dense cores; we then expect centrifugal radii of $R_c \gtrsim 100$ AU for typical stellar masses of 0.5–1.0 $M_\odot$ and consider the range $R_c = 10$–1000 AU. Table 6 summarizes the properties for our model grid.

TABLE 6

MODEL PARAMETERS

Model	$\dot{M}$ ($M_\odot$ yr^{-1})	R_c (AU)	θ_H	τ_K ($\mu = 0.5$)	Fits Data?
MRN1	1.0×10^{-6}	10	26	1.5	y
MRN2	2.0×10^{-6}	10	26	3.1	y
MRN3	5.0×10^{-6}	10	26	7.7	n
MRN4	4.6×10^{-6}	40	31	3.3	y
MRN5	5.0×10^{-6}	50	26	3.3	y
MRN6	2.0×10^{-6}	100	none	1.3	y
MRN7	5.0×10^{-6}	100	none	3.2	y
MRN8	2.5×10^{-6}	100	11	1.4	y
MRN9	5.0×10^{-6}	100	26	2.3	y
MRN10	5.0×10^{-6}	100	11	2.6	y
MRN11	5.0×10^{-6}	100	11	2.6	y
MRN12	5.0×10^{-6}	100	11	2.8	y
MRN13	1.0×10^{-5}	100	11	5.6	n
MRN14	5.0×10^{-6}	200	26	1.2	y
MRN15	5.0×10^{-6}	300	26	1.3	y
MRN16	9.2×10^{-6}	300	37	1.9	y
MRN17	9.2×10^{-6}	300	26	2.3	y
MRN18	1.3×10^{-5}	300	26	3.0	n
MRN19	5.0×10^{-6}	1000	26	0.6	y
MRN20	1.0×10^{-5}	1000	11	1.5	y
MRN21	1.0×10^{-5}	1000	11	1.6	y
MRN22	2.0×10^{-5}	1000	26	2.3	n
PTW1	2.5×10^{-6}	100	11	5.2	n
PTW2	5.0×10^{-6}	100	11	10.5	n

NOTES.—θ_H is the opening angle of outflow cavity, in degrees.
Model MRN11 uses a high albedo at K, $\omega = 0.3$.
The shape of the outflow cavity varies as $\varpi^{1.5}$ for models MRN10, MRN11, MRN18, and MRN21.

Each model consists of calculations at J, H, and K for each inclination angle, μ. For the input spectrum, we adopt model fluxes for a reprocessing disk surrounding an M0 T Tauri star at the distance of the Taurus cloud: $J_0 = 7.70$, $H_0 = 6.93$, and $K_0 = 6.50$ ($L_{bol} \approx 4\ L_\odot$). We ran 20 million photons through the Monte Carlo code to achieve good signal-to-noise in the output images and then summed the output flux in circular apertures having diameters of 8″, 13″, and 26″ to compare model colors with the SQIID data (assuming a distance to Taurus of 140 pc). We then normalized the resulting flux to the input magnitudes {i.e., $J = J_0 - 2.5 \log [F(\mu)/F_0]$, where F_0 is the input flux and $F(\mu)$ is the output flux for direction μ}. We convolved model images with a stellar point source from a SQIID image to approximate instrumental broadening. To match model and observed images for specific objects, we use the bolometric luminosity, L_{bol} (Table 1), to correct the fluxes of the input T Tauri spectrum and then use the zero points of the SQIID calibration to scale the output images. Finally, we compute the extinction at each viewing angle using a direct numerical integration of the optical depth through the envelope and by computing the ratio of the unscattered output flux to the input flux for each inclination bin. These two estimates agree except for edge-on envelopes ($\mu = 0$), where our bin size, $\delta\mu = 0.1$, is too coarse to resolve the steep variation in optical depth as a function of inclination angle.

3.2. *Comparison of Models and Observations: Near-Infrared Colors*

We begin with our "standard" model (MRN12 in Table 6): $\dot{M} = 5 \times 10^{-6}\ M_\odot$ yr^{-1}, $R_c = 100$ AU, MRN dust grains, and

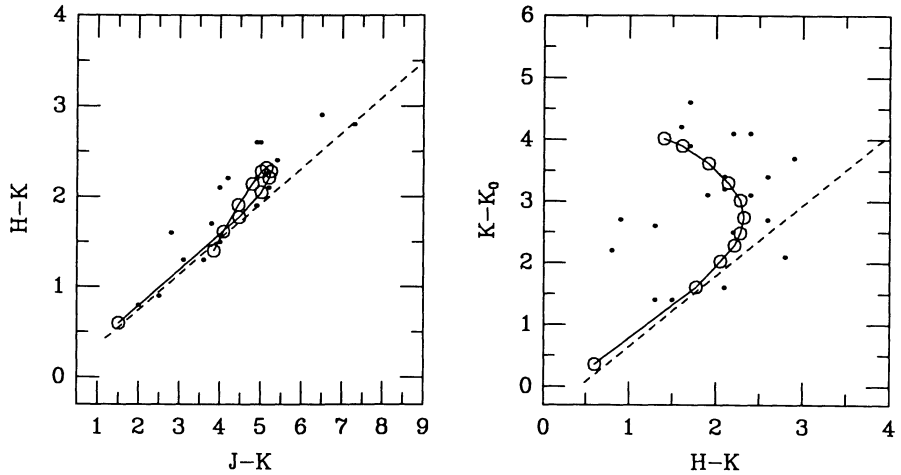

FIG. 6.—*Left panel*: color-color diagram for our standard scattering model (MRN12). The large open circles connected by the solid line plot model colors for inclinations ranging from $\mu \equiv \cos i = 1$ at $(J-K = 1.5, H-K = 0.6)$ to $\mu = 0$ in steps of 0.1. The inclination increases (μ decreases) counterclockwise around the loop. The observed colors for embedded sources are shown as small filled circles, while the dotted line plots a reddening line for MRN grains. *Right panel*: color-extinction diagram for the same model. The inclination increases from $\mu = 1$ to $\mu = 0$ in a counterclockwise direction around the loop. The dotted line shows the reddening line for pure extinction ($A_K = K_u - K_0$) for MRN grains.

a small opening angle, $\theta_H = 11°$, for the bipolar cavity. Figure 6 (*left panel*) compares our model $H-K$ and $J-K$ colors in a 13″ aperture with data for the embedded sources. Table 7 lists the magnitudes of the total flux, along with the unscattered flux from the central source, integrated in two apertures. The model colors trace a looping trajectory in the color-color plot, with inclination increasing counterclockwise along the loop. The dashed curve shows a reddening line for standard interstellar dust starting from the input disk colors. Both the models and the data lie mostly above the reddening line. Pole-on sources with $\mu = 0.975$ appear close to the colors of the reprocessing disk, because stellar photons have a fairly clear path to the observer. The model colors become redder with increasing inclination until $\mu \sim 0.5$ ($i = 60°$), because the extinction of the central object increases. Although the extinction to the central object continues to increase with inclination for $\mu < 0.5$, the

TABLE 7

MODEL RESULTS (MRN12)

	TOTAL FLUX			UNSCATTERED FLUX			SCATTERED FLUX			POLARIZATION		
μ	J	H	K	J_u	H_u	K_u	$F_{s,J}$	$F_{s,H}$	$F_{s,K}$	P_J	P_H	P_K
13″ Aperture												
0.0	14.36	11.91	10.52	34.00	22.20	14.64	100.0%	100.0%	97.8%	−39.0%	−33.0%	−21.0%
0.1	14.49	12.02	10.40	26.63	17.92	12.36	100.0	99.6	83.5	−38.0	−32.0	−17.0
0.2	14.57	12.03	10.12	22.68	15.62	11.14	100.0	96.3	60.9	−36.0	−29.0	−11.0
0.3	14.60	11.95	9.80	20.43	14.32	10.44	99.6	88.7	44.4	−33.0	−24.0	−7.1
0.4	14.53	11.80	9.52	18.91	13.44	9.97	98.6	77.2	34.0	−29.0	−18.0	−4.4
0.5	14.38	11.57	9.24	17.65	12.70	9.58	94.8	65.6	26.5	−23.0	−13.0	−2.7
0.6	14.23	11.27	8.99	16.61	12.10	9.26	89.2	53.5	21.5	−20.0	−8.9	−1.7
0.7	13.99	11.00	8.79	15.81	11.64	9.01	81.8	45.8	18.2	−14.0	−6.0	−1.2
0.8	13.54	10.58	8.53	14.82	11.06	8.70	68.0	35.2	14.9	−10.0	−3.8	−0.8
0.9	12.58	9.89	8.11	13.32	10.19	8.24	45.0	24.1	11.1	−5.4	−2.1	−0.5
0.975	8.36	7.46	6.86	9.09	7.74	6.93	13.0	10.3	6.6	−0.2	−0.2	−0.1
26″ Aperture												
0.0	13.72	11.54	10.28	34.00	22.20	14.64	100.0	100.0	98.2	−40.0	−35.0	−22.0
0.1	13.86	11.63	10.20	26.63	17.92	12.36	100.0	99.7	86.3	−39.0	−34.0	−19.0
0.2	13.95	11.67	9.97	22.68	15.62	11.14	100.0	97.4	65.8	−37.0	−32.0	−13.0
0.3	14.00	11.63	9.70	20.43	14.32	10.44	99.8	91.5	49.3	−34.0	−26.0	−8.8
0.4	13.96	11.53	9.45	18.91	13.44	9.97	99.2	82.1	38.3	−31.0	−21.0	−5.7
0.5	13.88	11.37	9.19	17.65	12.70	9.58	96.7	71.5	30.1	−25.0	−15.0	−3.7
0.6	13.81	11.12	8.95	16.61	12.10	9.26	92.7	59.8	24.3	−21.0	−11.0	−2.3
0.7	13.64	10.88	8.76	15.81	11.64	9.01	86.8	51.2	20.6	−15.0	−7.1	−1.5
0.8	13.30	10.50	8.50	14.82	11.06	8.70	74.4	39.8	16.7	−11.0	−4.4	−1.0
0.9	12.46	9.84	8.10	13.32	10.19	8.24	50.7	26.9	12.4	−5.7	−2.3	−0.6
0.975	8.35	7.45	6.85	9.09	7.74	6.93	13.3	10.8	7.0	−0.2	−0.2	−0.1

NOTES.—The total flux assumes input magnitudes of $J_0 = 7.7$, $H_0 = 6.93$, and $K_0 = 6.5$ for the central T Tauri star.
The sign of the polarization is negative if the position angle is perpendicular to the outflow axis, and positive for position angle parallel to this axis.

model colors become bluer again at higher inclinations ($\mu \sim 0.5$–0.0). This behavior occurs because the J and H flux—which are dominated by the scattering component—change relatively little, while the K flux continues to decrease (Table 7, cols. [2]–[4]).

The unscattered magnitudes in Table 7—J_u, H_u, and K_u—measure the line-of-sight extinction to the central source; we estimate $A_V \sim 90$ mag for $\mu = 0$, which agrees with the $A_V \sim 100$ mag estimated from submillimeter fluxes of typical embedded sources (Barsony & Kenyon 1992). The total (scattered + direct) flux suggests smaller extinctions, $A_V \sim 45$ mag, so observed near-IR colors underestimate the true line-of-sight reddening to the central source. Scattered light always contributes a significant amount to the K light and actually dominates the J and H fluxes for most inclination angles. As we will continue to show with additional models, *scattered light determines the near-IR colors of embedded sources* (see also ALS; Paper I).

The right panel of Figure 6 plots the "apparent extinction", $K - K_0$, as a function of $H - K$ for our standard model and the observations. The parabolic trajectory of the models—with μ decreasing (i increasing) counterclockwise around the curve—is again caused by the competition between extinction and scattering. Scattering dominates the H flux at high inclinations ($\mu = 0.0$–0.5) and produces blue $H - K$ colors as the K flux decreases; the direct flux from the central source begins to dominate at lower inclinations ($\mu = 0.5$–1.0), so the colors follow a standard reddening line. The true line-of-sight extinction to the central source—$K_0 - K_u$—increases monotonically from ~ 0.4 mag at $\mu = 0.975$ to 8.1 mag at $\mu = 0$ (Table 7). Approximately 2% of the emitted K flux scatters into a given direction in this model, so the apparent extinction never exceeds 4.0 mag at K.

Figures 7–8 show how our observable quantities change when we vary input parameters from their "standard" values. (Table 8 lists selected model results for the 13″ and 26″ apertures [Ap] at $\mu = 0.0$ and 0.5). The upper panels in Figure 7 demonstrate that we can account for most of the observed range in colors and apparent extinction simply by varying the opening angle of the polar hole from $\theta_H = 0°$ (no hole; *circles*) to $\theta_H = 26°$ (*triangles*). Models without bipolar holes produce the reddest colors, because the envelope reddens scattered light on its way out of the cloud. Similarly, the larger hole produces blue colors because the scattered flux suffers less reddening through the envelope. The $H - K$ and $J - K$ colors for many of our edge-on models fall below the reddening line. Scattering produces all of the observed flux at this inclination, even at K, and the model colors seem consistent with single-scattering plus reddening. For single scattering, the flux is proportional to the scattering opacity $\omega\kappa$. The intrinsic $J - K$ color for scattering is

$$J_s - K_s = J_0 - K_0 - 2.5 \log [(\omega_J \kappa_J)/(\omega_K \kappa_K)]$$
$$= (J_0 - K_0 - 2) \approx -0.8 ;$$

similarly

$$H_s - K_s = (H_0 - K_0 - 1.2) \approx -0.8 .$$

Thus, we need an extinction to the *scatterers* of $A_K \lesssim 3$ mag to match observed colors of the reddest sources with $J - K \sim 6$.

Models without polar holes can account for the observed range in the apparent extinction if we vary the infall rate, $\dot{M}$, and keep R_c fixed, but generally the predicted near-IR colors follow the reddening line in the color-color diagram (Fig. 7; *middle panels*). The optical depth through the envelope scales as $\dot{M} R_c^{-1/2}$, so the model colors still lie on the reddening line if we vary R_c and keep the infall rate fixed at any $\dot{M} \gtrsim 2 \times 10^{-6}$ $M_\odot$ yr^{-1}. Many embedded sources have $J - K$, $H - K$ colors well above the standard reddening line; thus, we conclude that scattering models using the TSC density distribution cannot reproduce the observed colors (unless we make the ad hoc assumption that the reddening law varies significantly from cloud to cloud).

The lower panels of Figure 7 show how our observable quantities change when we vary the infall rate, $\dot{M}$, from 2.5×10^{-6} $M_\odot$ yr^{-1} (*triangles*) to 10^{-5} $M_\odot$ yr^{-1} (*circles*) and keep other parameters at their standard values. The models produce redder colors and larger $K - K_0$ for higher infall rates at constant R_c, because the envelope density—and thus the optical depth through the envelope—increases with increasing infall rate. Infall rates much larger than $\dot{M} \sim 7$–8×10^{-6} $M_\odot$ yr^{-1} produce apparent extinctions, $K - K_0$, much larger than those observed for $R_c \sim 100$ AU.

We can place good constraints on the centrifugal radius by considering two sets of models. First, the upper panels of Figure 8 show results for envelopes with a constant optical depth to the central source (i.e., $\tau \propto \dot{M} R_c^{-1/2} \approx$ constant). Although we might expect roughly similar colors and extinctions for envelopes with constant τ, the large R_c model fails to reproduce the observations in the $H - K$ versus $K - K_0$ diagram by a large factor at high inclinations ($\mu \lesssim 0.6$). However, this conclusion depends on our choice for the photometric aperture. Most of the scattered flux in all of our models escapes the envelope *outside* the centrifugal radius, where the density gradient changes from $\rho \propto r^{-1/2}$ to $\rho \propto r^{-3/2}$ (see eq. [1]). Our standard aperture, $r \sim 1000$ AU, thus includes most of the scattered light for small R_c models but excludes this radiation as R_c approaches 1000 AU. The colors for the small R_c models are therefore dominated by scattered light and appear much bluer than those for the large R_c models which are dominated by direct light reddened by the envelope. Table 8 shows large differences in the colors and magnitudes between the medium and large apertures in the large R_c model (MRN22).

We can understand this result more clearly by examining the optical depth integrated along chords to the polar axis at constant distance above the midplane. For simplicity, we can imagine that most of the scattering occurs in the polar regions where the optical path is lower and then compute the optical depth from these scatterers to an observer viewing the object edge-on. Figure 9 (*left panel*) plots the extinction at various impact parameters, h, above the midplane for the three models in the top panels of Figure 8. We derived above that we need $A_K \lesssim 3$ mag to the scatterers to reproduce the observed colors, $J - K \lesssim 6$, if 100% of the emergent light is scattered. Most sources have $J - K \lesssim 5$. The models that reproduce these colors have some direct (redder) light, so the extinction to the scatterers should be around $A_K \lesssim 2$ mag. Both the $R_c = 100$ AU and $R_c = 300$ AU envelopes have $A_K \leq 2$ over some range of $h \leq 6\farcs5$—our standard aperture size—whereas A_K falls below 2 mag only for our largest aperture, $h \sim 13''$, when $R_c = 1000$ AU. Thus, the model colors for the $R_c = 1000$ AU envelope appear much redder than the observed colors for high infall rates.

We now consider models where we change R_c and keep the infall rate fixed. Recalling equation (1), the density approaches

the spherical infall limit for $r \gg R_c$, so the density in the outer envelope is essentially independent of R_c. Thus, we can keep the extinction *in our standard aperture* roughly constant and test the sensitivity of the apparent K extinction to R_c. Figure 9 (*right panel*) shows the extinction at different impact parameters for several values of R_c with $\dot{M}$ held constant; A_K varies slightly outside $h = 6''.5$ only because the size of the bipolar cavity increases with increasing R_c. All of these models produce low A_K at $h = 6''.5$ and thus meet one basic requirement of the data. However, the extinction inside R_c varies considerably between these models, because the density gradient switches from $\rho \propto r^{-3/2}$ to $\rho \propto r^{-1/2}$ at $r \sim R_c$. Thus, the small R_c models are more centrally condensed and produce larger K extinctions than large R_c models. In fact, the K extinction to the central object is so low for $R_c \geq 300$ AU that the reddened stellar flux dominates over scattering and the colors fall very close to the reddening line (Fig. 8; *middle panel*).

We find that a range in R_c and $\dot{M}$ can fit our observed colors (Fig. 8; *upper and middle panels*). The extinction to the emitting source must be large enough to obscure most of the stellar flux, yet the extinction in the regions subtended by the aperture must be low enough for scattered flux to be transmitted. Thus, the density distribution must be centrally condensed. *The colors of the embedded sources in Taurus-Auriga preclude models with very large centrifugal radii,* $R_c \gtrsim 1000$ AU, *and high infall rate,* $\dot{M} \gtrsim 10^{-5}\ M_\odot\ \mathrm{yr}^{-1}$ (see Table 2). This result

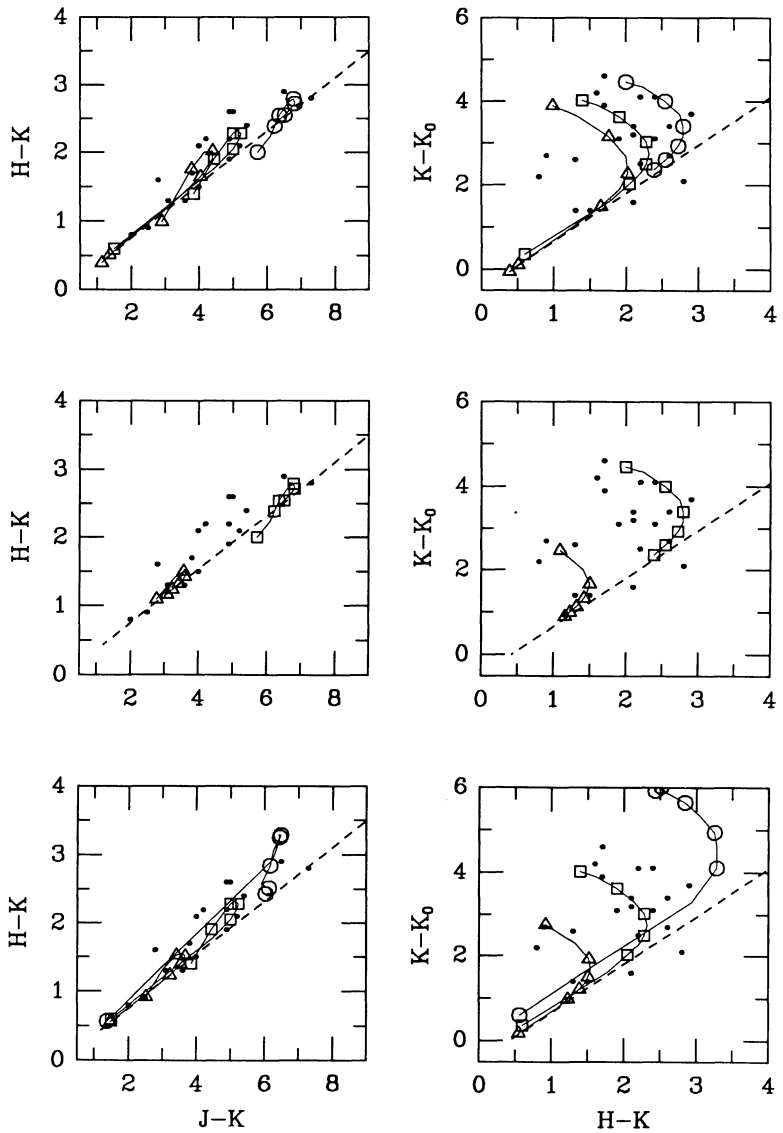

FIG. 7.—Color-color and color-extinction diagrams for various scattering models. Each panel plots observed colors as small filled circles and the reddening curve as a dashed line. As in Fig. 6, each model follows a loop as the inclination varies from $\mu = 1$ to $\mu = 0$ in steps of 0.2. *Upper panels*: models with opening angles for polar holes of $\theta_H = 0°$ (no hole; circles; MRN7), 11° (*squares*; MRN12), and 26° (*triangles*; MRN9). *Middle panels*: models with $\theta_H = 0°$ and two infall rates: $\dot{M} = 5 \times 10^{-6}\ M_\odot\ \mathrm{yr}^{-1}$ (*squares*; MRN7) and $\dot{M} = 2 \times 10^{-6}\ M_\odot\ \mathrm{yr}^{-1}$ (*triangles*; MRN6). *Lower panels*: models with $\theta_H = 11°$ and varying $\dot{M}$. The reddening increases as the infall rate increases from $\dot{M} = 2.5 \times 10^{-6}\ M_\odot\ \mathrm{yr}^{-1}$ (*triangles*; MRN8) to $\dot{M} = 5 \times 10^{-6}\ M_\odot\ \mathrm{yr}^{-1}$ (*squares*; MRN12) to $\dot{M} = 1 \times 10^{-5} M_\odot\ \mathrm{yr}^{-1}$ (*circles*; MRN13).

appears to be independent of the shape of the outflow cavity, at least for the range of cavity properties listed in Table 6. The large R_c models can fit the data only with a narrow range of infall rate and inclination. Model MRN21, with $R_c = 1000$ AU, produces colors well above the reddening line only for large inclinations, $\mu = 0.0$–0.3 ($i \gtrsim 72°$). A larger infall rate results in apparent extinctions, $K - K_0$, larger than we observe (e.g., model MRN22). The colors for models with lower infall rates fall on the reddening line; however, these objects have less opaque envelopes and probably cannot produce broad spectral energy distributions that peak at wavelengths exceeding 20 μm (Paper I). Models with $R_c \sim 300$ AU and $\dot{M} \sim 10^{-5}\ M_\odot\ \mathrm{yr}^{-1}$ can account for the colors and extinctions of several very red sources in Taurus-Auriga, but most objects have blue colors and lower apparent extinctions than implied by these dense models (see below).

Aside from these results, the models predict that near-IR colors become bluer with increasing aperture size because all the extra flux in a larger beam is blue (scattered) light. The amount of bluing with aperture size in the model images varies with R_c (Table 8). While the change in $J - K$ between the 13″ and 26″ apertures in the observed images is usually less than 0.1 mag (Table 2), the model images have this small range only when $R_c \sim 10$ AU. The difference in $J - K$ between our smallest and largest apertures ranges from 0.1–0.5 mag, while the $J - K$ color can decrease by as much as 1–2 mag for $R_c = 1000$ AU. However, the signal-to-noise of the scattered light in the observed images is very low at distances of $\sim 10''$ from the central point source, which complicates our interpretation. Higher quality images could potentially allow us to measure R_c from the observed change in color as a function of aperture size. Even with this caveat, none of our models can account for

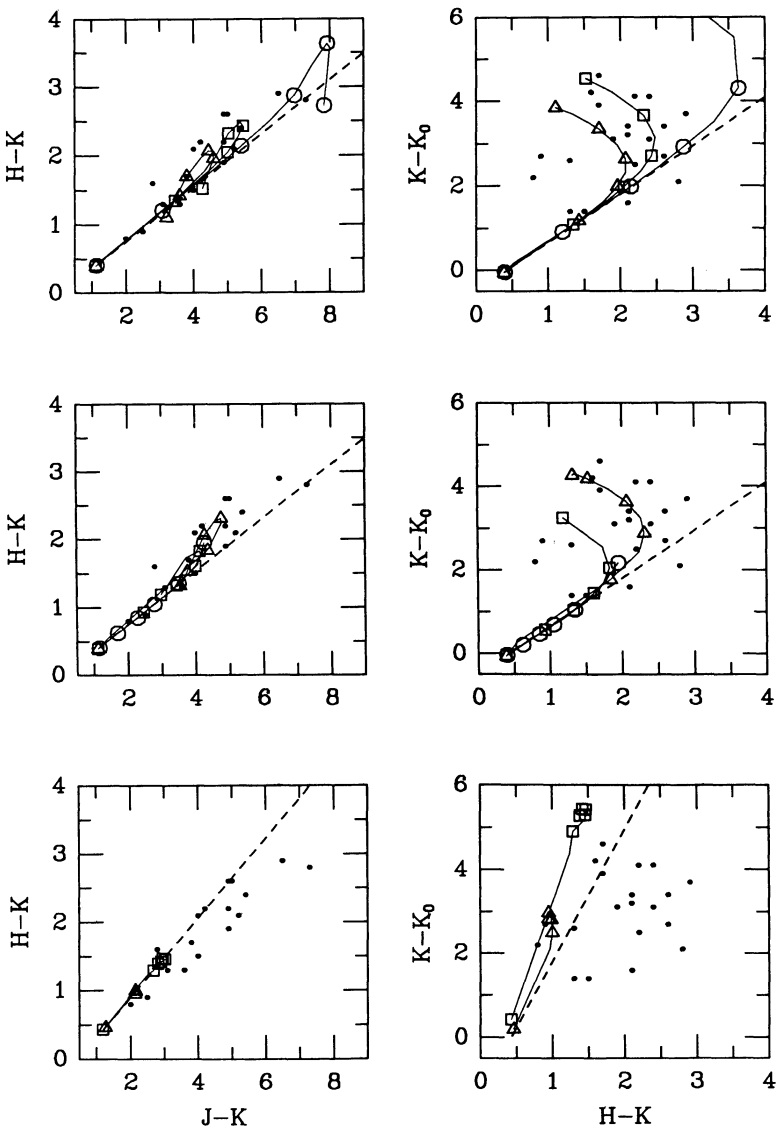

FIG. 8.—Same as in Fig. 7 for several scattering models. *Upper panels*: models with similar optical depth ($\tau \propto \dot{M} R_c^{-1/2}$). The models increase in reddening (from left to right) as R_c increases from $R_c = 100$ AU (*triangles*; MRN9) to $R_c = 300$ AU (*squares*; MRN17) to $R_c = 1000$ AU (*circles*; MRN22). *Middle panels*: models with constant $\dot{M}$ and varying R_c. The models follow the reddening line more closely as R_c increases from $R_c = 50$ AU (*triangles*; MRN5) to $R_c = 300$ AU (*squares*; MRN15) to $R_c = 1000$ AU (*circles*; MRN19). *Lower panels*: models using PTW grains for $\dot{M} = 2.5 \times 10^{-6} M_\odot\ \mathrm{yr}^{-1}$ (*triangles*; PTW1) and $\dot{M} = 5 \times 10^{-6}\ M_\odot\ \mathrm{yr}^{-1}$ (*squares*; PTW2).

TABLE 8

MODEL RESULTS, SELECTED INCLINATIONS

			EMERGENT FLUX				SCATTERED FLUX			POLARIZATION		
MODEL	μ	APERTURE	$J-K$	$H-K$	K	$K-K_0$	$F_{s,J}$	$F_{s,H}$	$F_{s,K}$	P_J	P_H	P_K
MRN1	0.0	13″	2.00	0.65	9.32	2.82	100.0%	99.6%	87.1%	−20.0%	−13.5%	−4.0%
		26	1.91	0.61	9.27	2.77	100.0	99.6	87.7	−20.0	−14.0	−4.4
	0.5	13	3.43	1.48	8.01	1.51	82.3	47.5	18.9	−12.9	−4.6	−0.3
		26	3.34	1.46	8.00	1.50	83.8	49.2	19.6	−13.3	−4.9	−0.4
MRN2	0.0	13	2.73	1.04	10.31	3.81	100.0	100.0	99.5	−33.0	−29.0	−17.1
		26	2.53	0.98	10.22	3.72	100.0	100.0	99.5	−33.0	−29.0	−17.7
	0.5	13	3.87	1.96	9.50	3.00	99.3	84.1	35.7	−26.0	−19.4	−4.6
		26	3.65	1.88	9.47	2.97	99.4	85.7	37.4	−26.0	−20.0	−5.0
MRN3	0.0	13	3.47	1.43	12.37	5.87	100.0	100.0	100.0	−38.0	−46.0	−42.0
		26	3.08	1.28	12.16	5.66	100.0	100.0	100.0	−39.0	−45.0	−43.0
	0.5	13	3.54	1.53	12.56	6.06	100.0	99.9	91.4	−35.0	−37.0	−31.0
		26	3.13	1.36	12.39	5.89	100.0	100.0	92.6	−32.0	−36.0	−31.0
MRN4	0.0	13	3.30	1.25	10.73	4.23	100.0	100.0	99.8	−25.0	−23.0	−12.8
		26	2.85	1.07	10.51	4.02	100.0	100.0	99.8	−27.0	−24.0	−14.3
	0.5	13	4.36	2.21	9.73	3.23	99.1	81.7	31.4	−27.0	−18.3	−3.6
		26	3.88	2.02	9.67	3.17	99.4	85.5	35.1	−26.0	−19.5	−4.3
MRN5	0.0	13	3.54	1.32	10.76	4.26	100.0	100.0	99.8	−31.0	−28.0	−16.7
		26	3.01	1.14	10.53	4.03	100.0	100.0	99.8	−33.0	−29.0	−18.7
	0.5	13	4.55	2.26	9.75	3.25	99.0	81.4	32.0	−28.0	−20.0	−4.2
		26	4.05	2.06	9.69	3.19	99.4	85.6	36.0	−28.0	−21.0	−5.2
MRN6	0.0	13	2.77	1.09	8.97	2.47	99.8	94.9	59.4	−16.2	−12.7	−4.8
		26	2.57	0.98	8.89	2.39	99.8	95.7	62.4	−16.7	−13.5	−5.5
	0.5	13	3.53	1.37	7.72	1.22	61.2	35.9	15.3	−4.8	−1.9	−0.2
		26	3.43	1.34	7.70	1.20	65.3	39.0	16.7	−5.7	−2.4	−0.4
MNR7	0.0	13	5.72	2.00	10.96	4.46	100.0	99.9	97.5	−19.0	−27.0	−20.0
		26	5.45	1.92	10.75	4.25	100.0	100.0	98.0	−22.0	−27.0	−21.0
	0.5	13	6.78	2.79	9.65	3.15	90.6	65.0	29.1	−12.6	−9.1	−2.6
		26	6.56	2.69	9.61	3.11	92.6	69.3	32.0	−13.8	−10.3	−3.2
MRN8	0.0	13	2.52	0.92	9.25	2.75	99.9	98.1	71.4	−22.0	−16.3	−5.7
		26	2.29	0.81	9.13	2.63	100.0	98.5	74.4	−24.0	−17.7	−6.9
	0.5	13	3.62	1.46	7.85	1.35	67.2	37.6	15.5	−9.1	−3.0	−0.3
		26	3.46	1.41	7.82	1.32	72.4	41.8	17.3	−10.7	−4.0	−0.5
MRN9	0.0	13	3.20	1.10	10.34	3.84	100.0	100.0	96.8	−23.0	−17.4	−7.3
		26	2.70	0.93	10.07	3.57	100.0	100.0	97.5	−25.0	−20.0	−9.7
	0.5	13	4.59	2.07	8.81	2.31	90.6	53.3	19.4	−21.0	−7.9	−0.9
		26	4.11	1.92	8.76	2.26	94.3	61.1	22.9	−22.0	−10.2	−1.5
MRN10	0.0	13	2.99	1.06	10.40	3.90	100.0	100.0	97.8	−31.0	−26.0	−13.9
		26	2.40	0.83	10.10	3.60	100.0	100.0	98.4	−35.0	−31.0	−18.0
	0.5	13	4.38	2.09	9.08	2.58	96.2	66.2	23.8	−23.0	−12.7	−1.8
		26	3.72	1.85	9.01	2.51	98.0	74.5	28.2	−26.0	−16.6	−3.0
MRN11	0.0	13	3.47	1.54	9.92	3.42	100.0	100.0	98.6	−31.0	−26.0	−12.8
		26	2.89	1.32	9.61	3.11	100.0	100.0	99.0	−35.0	−31.0	−16.6
	0.5	13	4.51	2.23	8.94	2.44	96.2	66.2	33.0	−23.0	−12.7	−2.3
		26	3.89	2.02	8.85	2.35	98.0	74.5	38.5	−26.0	−16.6	−3.9
MRN12	0.0	13	3.85	1.40	10.52	4.02	100.0	100.0	97.8	−39.0	−33.0	−21.0
		26	3.45	1.26	10.28	3.78	100.0	100.0	98.2	−40.0	−35.0	−22.0
	0.5	13	5.13	2.32	9.24	2.74	94.8	65.6	26.5	−23.0	−13.2	−2.7
		26	4.69	2.18	9.19	2.69	96.7	71.5	30.1	−25.0	−15.5	−3.7
MRN13	0.0	13	6.04	2.43	12.42	5.92	100.0	100.0	100.0	−45.0	−52.0	−43.0
		26	5.11	2.01	12.03	5.53	100.0	100.0	100.0	−50.0	−56.0	−44.0
	0.5	13	6.26	3.05	11.83	5.33	100.0	96.4	54.1	−35.0	−31.0	−12.8
		26	5.29	2.63	11.67	5.17	100.0	97.9	60.5	−35.0	−34.0	−15.8
MRN14	0.0	13	2.59	0.95	10.36	3.86	100.0	99.7	81.2	0.9	5.6	10.0
		26	1.85	0.60	9.94	3.44	100.0	99.8	87.2	−4.8	0.3	6.6
	0.5	13	3.64	1.42	7.66	1.16	32.8	16.5	7.6	−0.7	0.9	0.9
		26	3.40	1.36	7.64	1.14	47.7	22.9	9.7	−3.1	0.2	0.8
MRN15	0.0	13	2.98	1.19	9.75	3.25	99.9	97.1	62.3	−7.8	−1.4	3.6
		26	2.37	0.87	9.46	2.96	100.0	98.4	71.1	−12.0	−5.4	1.8
	0.5	13	3.75	1.48	7.75	1.25	42.4	21.3	9.0	−3.0	0.1	0.7
		26	3.50	1.41	7.71	1.21	55.5	28.4	11.7	−5.6	−0.9	0.5
MRN16	0.0	13	2.90	0.99	10.39	3.89	100.0	99.9	95.3	−9.1	−3.3	3.5
		26	2.43	0.81	10.09	3.59	100.0	100.0	96.4	−11.1	−5.8	1.4
	0.5	13	4.40	1.91	8.40	1.90	75.5	36.3	13.5	−11.7	−2.5	0.4
		26	4.00	1.80	8.36	1.86	83.5	43.9	16.1	−13.3	−3.9	0.2
MRN17	0.0	13	4.26	1.52	11.03	4.53	100.0	100.0	94.9	−16.0	−10.6	−2.3
		26	3.31	1.14	10.46	3.96	100.0	100.0	97.0	−21.0	−17.0	−6.6
	0.5	13	5.32	2.28	8.85	2.35	77.5	37.2	13.1	−16.1	−4.0	0.0
		26	4.62	2.09	8.78	2.28	88.8	50.1	17.9	−20.0	−7.3	−0.7

TABLE 8—*Continued*

Model	μ	Aperture	Emergent Flux				Scattered Flux			Polarization		
			$J-K$	$H-K$	K	$K-K_0$	$F_{s,J}$	$F_{s,H}$	$F_{s,K}$	P_J	P_H	P_K
MRN18	0.0	13	5.13	1.79	12.15	5.65	100.0	100.0	99.6	−9.2	−5.3	2.1
		26	3.47	1.20	11.17	4.67	100.0	100.0	99.8	−13.6	−12.5	−3.9
	0.5	13	5.82	2.65	9.34	2.84	84.2	37.0	11.5	−17.4	−3.8	0.2
		26	4.70	2.32	9.26	2.76	94.7	56.6	17.5	−22.0	−8.7	−0.6
MRN19	0.0	13	4.25	1.95	8.67	2.17	82.4	37.8	9.1	6.5	5.1	1.7
		26	3.00	1.46	8.53	2.03	95.1	65.2	20.3	2.7	5.5	3.1
	0.5	13	2.51	0.94	7.06	0.56	11.8	6.8	3.4	1.1	1.0	0.6
		26	2.43	0.91	7.04	0.54	19.8	11.3	5.3	0.9	1.1	0.7
MRN20	0.0	13	4.47	1.95	10.52	4.02	99.8	94.8	49.4	−18.6	−14.0	−2.9
		26	3.36	1.33	10.00	3.50	100.0	98.2	68.5	−23.0	−16.4	−5.2
	0.5	13	4.35	1.71	8.00	1.50	38.0	18.8	7.4	−2.1	0.1	0.5
		26	4.09	1.63	7.95	1.45	53.5	27.2	11.0	−5.8	−1.1	0.3
MRN21	0.0	13	4.59	1.95	10.62	4.12	99.8	95.9	52.3	−21.0	−15.3	−3.8
		26	3.45	1.34	10.10	3.60	99.9	98.6	70.4	−25.0	−18.3	−5.9
	0.5	13	4.55	1.79	8.12	1.62	45.5	22.0	8.4	−3.0	−0.0	0.5
		26	4.24	1.71	8.08	1.58	60.6	30.5	12.1	−7.3	−1.4	0.3
MRN22	0.0	13	7.8	2.72	13.17	6.67	100.0	99.1	84.2	10.0	0.8	5.4
		26	4.8	1.74	11.69	5.19	100.0	99.9	96.0	−15.0	−8.9	−0.5
	0.5	13	6.23	2.50	8.92	2.42	44.1	16.6	6.1	−7.6	−0.3	0.5
		26	5.44	2.34	8.87	2.37	74.4	31.8	10.8	−17.0	−3.4	0.2
PTW1	0.0	13	2.14	0.95	9.32	2.82	100.0	100.0	100.0	−3.9	−6.0	−8.1
		26	1.89	0.80	8.85	2.35	100.0	100.0	100.0	−4.0	−6.0	−8.3
	0.5	13	2.15	0.98	9.40	2.90	98.9	97.7	92.8	−2.8	−3.9	−4.6
		26	1.93	0.84	9.04	2.54	99.4	98.5	94.8	−2.9	−4.1	−5.2
PTW2	0.0	13	3.02	1.46	11.80	5.30	100.0	100.0	100.0	−3.4	−7.7	−11.8
		26	2.49	1.14	10.92	4.42	100.0	100.0	100.0	−3.8	−7.9	−11.7
	0.5	13	2.80	1.39	11.89	5.39	100.0	99.9	99.6	−4.2	−6.1	−9.6
		26	2.40	1.15	11.15	4.65	100.0	100.0	99.8	−3.9	−5.8	−9.2

NOTES.—The total flux assumes input magnitudes of $J_0 = 7.7$, $H_0 = 6.93$, and $K_0 = 6.5$ for the central T Tauri star.

The sign of the polarization is negative if the position angle is perpendicular to the outflow axis, and positive for position angle parallel to this axis.

The model polarizations have estimated uncertainties of $\pm 0.1\%$ for $p \lesssim 20\%$ and $\pm 1\%$ for $p \gtrsim 20\%$; the J polarizations for models MRN13 and MRN22 have uncertainties of $\pm 5\%$ due to low signal-to-noise in the output images.

the apparent *increase* in the $H-K$ and $J-K$ colors with increasing aperture size observed in 04361+2547 and 04365+2535.

Grains with radically different optical properties from MRN grains may not be capable of reproducing the observations. We calculated scattering models for the larger Pendleton, Tielens, & Werner (1990, hereafter PTW) grains, which have grayer opacities and much higher albedos than do the MRN grains. We consider our standard model and another model with a factor of 2 smaller infall rate (Table 6). The model colors lie along the PTW reddening line (Fig. 8; *lower panels*). However, this reddening line is much steeper than the standard MRN curve, so most of the observations now fall *below* the reddening line. These grains produce higher extinctions—$A_K \sim 20$ mag—

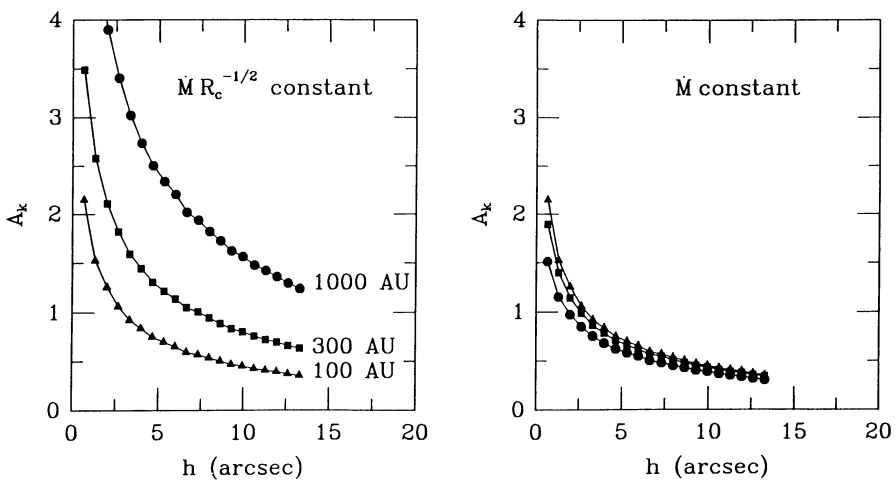

FIG. 9.—K-band extinction as a function of impact parameter, h, for the models shown in Fig. 8. *Left panel*: constant optical depth models (MRN9, MRN17, MRN22) in which R_c increases from $R_c = 100$ AU (*triangles*) to $R_c = 300$ AU (*squares*) to $R_c = 1000$ AU (*circles*). *Right panel*: constant infall rate models (MRN9, MRN15, MRN19) in which R_c increases as in the left panel.

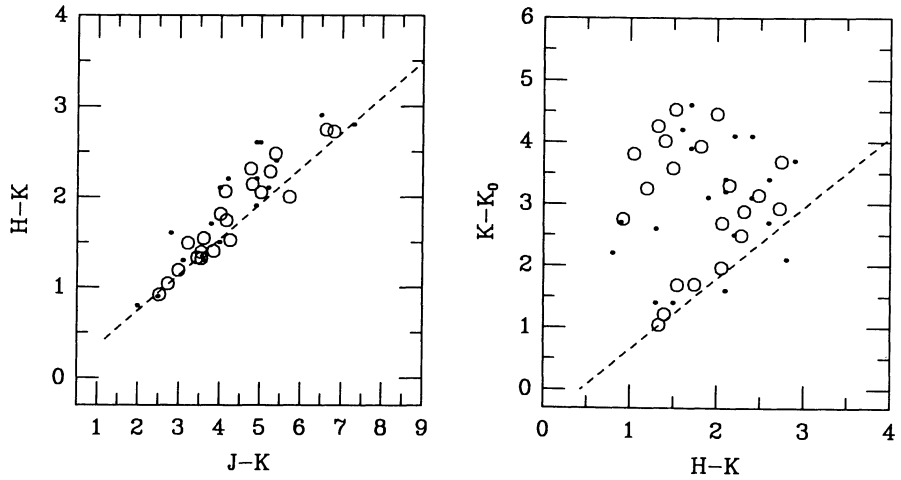

FIG. 10.—Color-color and extinction plots for several scattering models that agree with the embedded source data. For each model we plot the data for inclinations $\mu = 0, 0.3$, and 0.6.

than do MRN grains, but their higher albedos more than compensate for the lack of direct stellar flux in our models. Even so, the observed colors for the standard model are almost never as red as a typical embedded source, while the predicted $K-K_0$ is much larger than we observe in Taurus-Auriga. We can reduce the predicted $K-K_0$ by decreasing the infall rate (model PTW1 in Table 6), but this model results in even smaller $J-K$ and $H-K$ colors than PTW2. Thus, these grains appear too grey to match observations.

Figure 10 presents results for a range in model parameters about our standard model: $\dot{M} \sim 2$–$9 \times 10^{-6}\ M_\odot\ \mathrm{yr}^{-1}$, $R_c \sim$ 50–300 AU, and $\theta_H \sim 0°$–$37°$. We conclude that modest variations in envelope parameters and inclinations to the line of sight can account for the observed ranges in near-IR colors and $K-K_0$ among the embedded sources in Taurus-Auriga. As we noted above, the observed colors appear to preclude models with very large centrifugal radii, $R_c \gtrsim 1000$ AU, and high infall rate, $\dot{M} \gtrsim 10^{-5}\ M_\odot\ \mathrm{yr}^{-1}$. Our models also require bipolar holes in the rotating envelope; the scattered light in envelopes without bipolar holes is too heavily reddened to account for the range in colors and apparent extinctions observed in our sample for infall rates that reproduce the far-IR energy distributions. Fortunately, the colors do not vary considerably with the shape of the hole, although they do depend on the opening angle, θ_H (see Fig. 7). However, the near-IR colors and apparent extinctions do not provide robust estimates for the envelope parameters, because several sets of ($\dot{M}$, R_c, and i) can reproduce the observations. The extent of the scattered light nebula provides additional constraints on these parameters, so we now consider a comparison of model and real images.

3.3. *Comparison of Models with Observations: Near-Infrared Images*

As in § 3.2, we begin by demonstrating the need for an evacuated cavity in the rotating envelope. Figure 11 compares *JHK* images for an envelope with and without a bipolar hole using our "standard" values for $\dot{M}$ and R_c ($\dot{M} = 5 \times 10^{-6}\ M_\odot\ \mathrm{yr}^{-1}$; $R_c = 100$ AU) and an inclination of 90° (edge-on). The models with a bipolar cavity ($\theta_H = 26°$) produce images that resemble the observations presented in Figures 1–4. However, models without cavities appear much less extended than the observed sources at *H* and *K* and also emit much less radiation at *J* than detected in most sources. We could increase the amount of *J* flux produced by these models by reducing the envelope opacity (i.e., decreasing $\dot{M}R_c^{-1/2}$). In fact, model MRN6, which has no hole and an infall rate of $2 \times 10^{-6}\ M_\odot\ \mathrm{yr}^{-1}$ gives similar size images to the model with a hole and a factor 2.5 higher infall rate. Figure 12 contrasts *H*-band model images at three inclination angles. The extent of the scattered light nebulosity decreases with decreasing inclination in both cases, because the illuminated surface appears smaller in projection, as in a cone viewed pole-on. Yet, images in models with a bipolar cavity still appear extended at low inclinations, while images with no cavity closely resemble point sources. Several embedded sources—such as 04295+2251 and 04489+3042—have pointlike images at *JHK*, near-IR colors close to the reddening line, and no obvious molecular outflow; thus, these objects could possess rotating envelopes without a bipolar cavity. The remaining sources are either too extended or have near-IR colors too far away from the reddening line to be explained by envelopes without an evacuated bipolar cavity.

Changes to the hole geometry can increase the size of an image. Increasing the opening angle of the hole modifies the apparent elongation of the images, while the size of the extended nebulosity depends critically on the shape of the cavity. The streamline hole in our standard model asymptotically reaches a cone shape at large distance, so little emitted flux intercepts the hole "wall" on large scales. A curved hole [i.e., $z = 0.15\ (\varpi/1\ \mathrm{AU})^{1.5} - 0.93$ AU for $\varpi \gtrsim 3.5$ AU, where ϖ is the cylindrical radius] allows more direct stellar flux to intercept the envelope at large radii, which results in more scattered flux at larger distances and hence bigger images. Unfortunately, the large point spread function of the SQIID images (FWHM $\sim 2''$) makes it difficult to constrain the shape of the hole. Observations with better spatial resolution ($\lesssim 1''$) might provide a better test of the hole geometry.

Variations in the grain properties can also change the appearance of our model images. For example, more scattered light could be produced by increasing the albedo. We are reluctant to change the grain parameters significantly, because our adopted properties give reasonable colors, extinctions, and

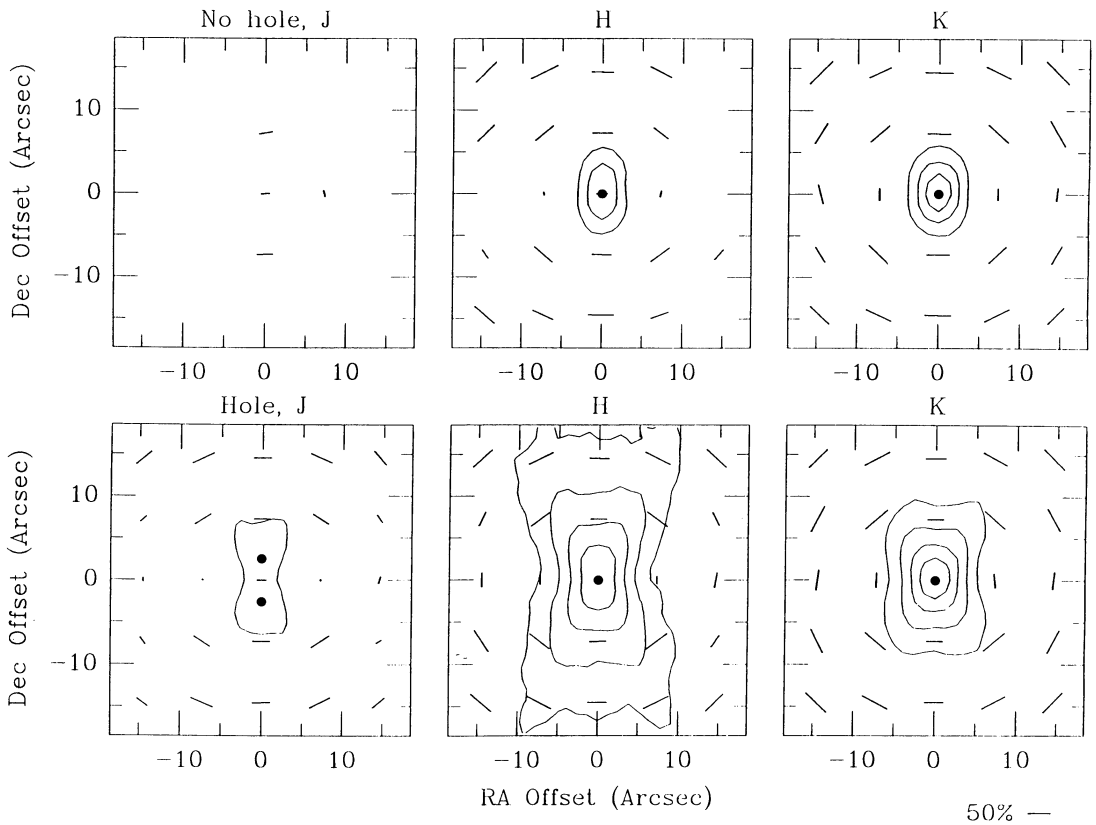

FIG. 11.—Model *JHK* images for envelopes with and without a bipolar cavity. Both sets of models assume $\dot{M} = 5 \times 10^{-6}\ M_{\odot}\ \mathrm{yr}^{-1}$, $R_c = 100$ AU, and $\mu = 0$ ($i = 90°$). The flux contours are spaced at intervals of 1 mag from peak intensity, which is indicated by a filled circle in each panel. Solid lines indicate polarization vectors; a vector with $p = 50\%$ appears in the lower right corner. *Upper panels*: *JHK* images for $\theta_H = 0°$ (no hole); *Lower panels*: *JHK* images for $\theta_H = 26°$.

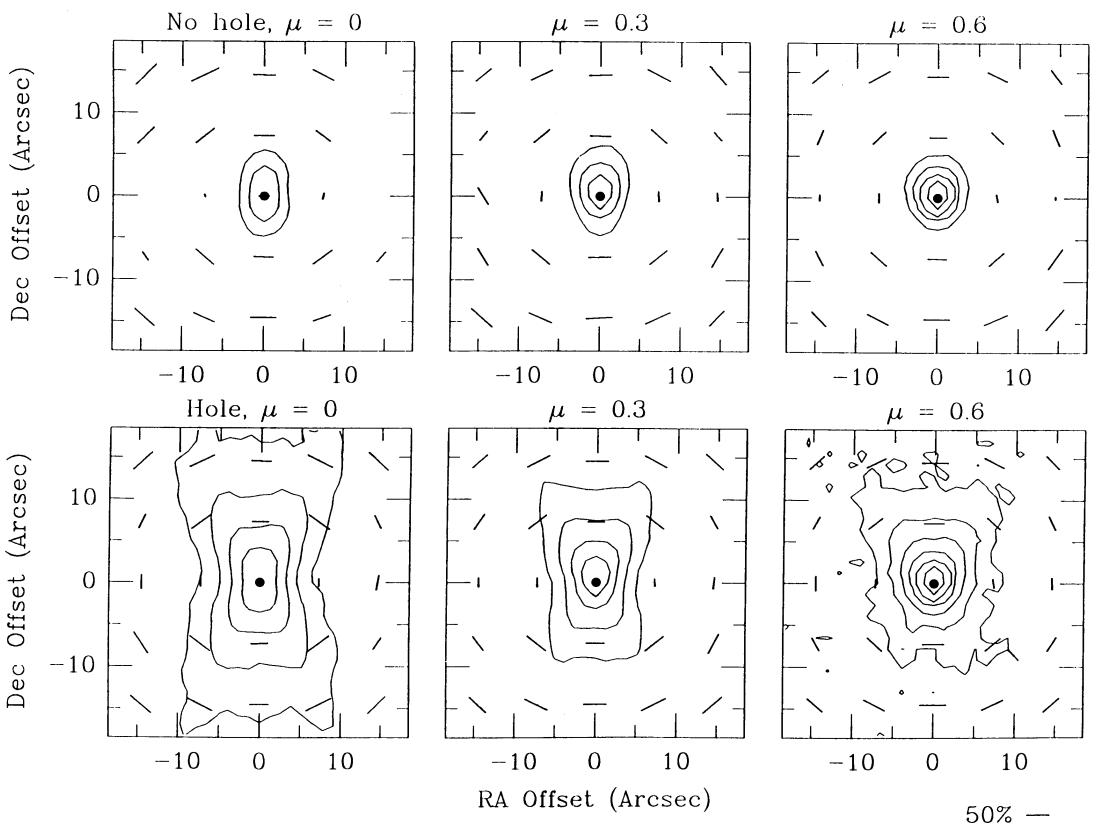

FIG. 12.—Same as in Fig. 11 for *H* images of envelopes at three inclination angles

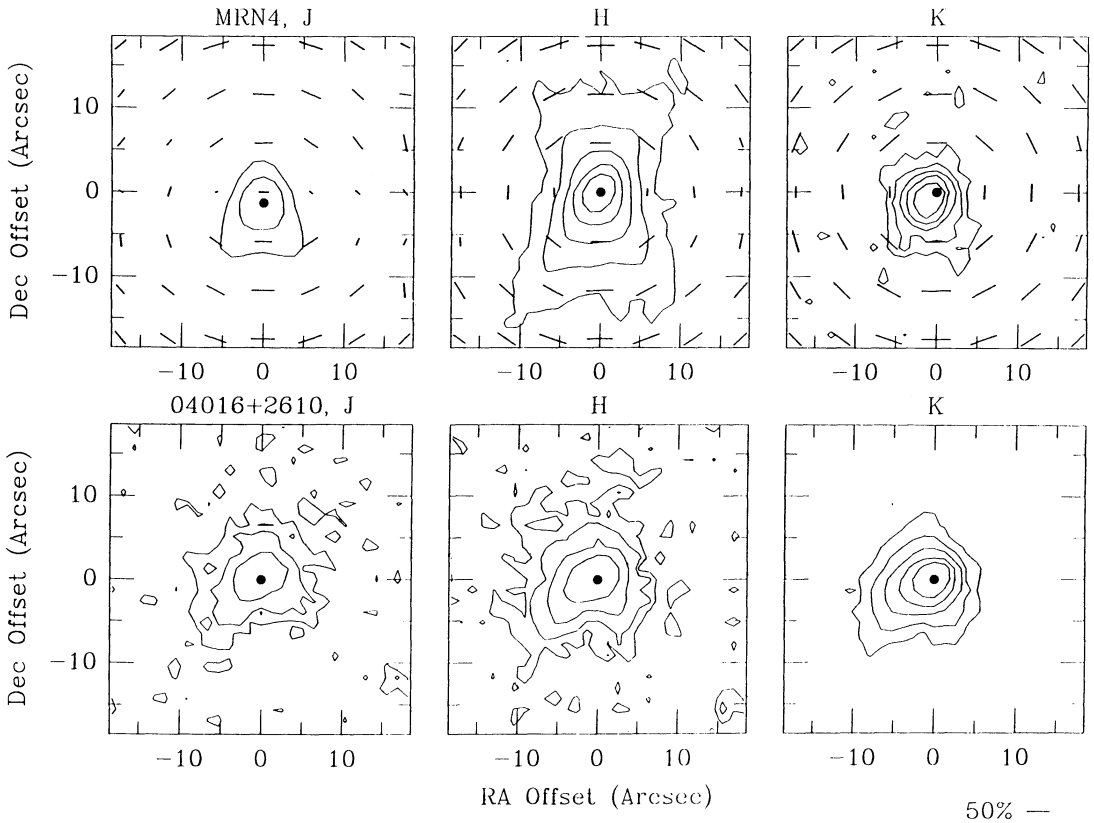

FIG. 13.—Comparison of model and observed images for the embedded *IRAS* source 04016+2610. *Upper panels*: *JHK* images for a model with $\dot{M} = 4.5 \times 10^{-6}$ $M_\odot$ yr^{-1}, $R_c = 40$ AU, $\theta_H = 31°$, and $i = 60°$. *Bottom panels*: *JHK* observations of 04016+2610.

polarizations. However, increasing the albedo at *K*, from $\omega = 0.2$ to $\omega = 0.3$, does increase the image size.

Figure 12 shows that the image morphology depends sensitively on the inclination. We do not have enough information on polarization and molecular outflows to model each source in detail, so we present one example of an attempt to produce model images similar to an observed source, 04016+2610. We first estimated ($\dot{M}$, R_c, and i) from the observed colors and then iterated these parameters until the model images resembled the observed images. We do not observe a large, rectangular nebula in 04016+2610—which our models produce for edge-on sources—so we tilt the model to produce a smaller, unipolar image. In general, we can decrease both i and R_c to produce the same near-IR colors; however, model images observed at low inclination appear smaller than those with large i. We find "best" model images and colors for an infall rate of $\sim 4.5 \times 10^{-6}$ $M_\odot$ yr^{-1}, $R_c \approx 40$ AU, and $i \approx 60°$; these parameters agree very well with Paper I's estimates ($\dot{M} \sim 4 \times 10^{-6}$ $M_\odot$ yr^{-1}, $R_c \sim 70$ AU, and $i \approx 60°$). Figure 13 compares a set of model images with our observations of 04016+2610. The image size is similar, but the morphology is not exactly the same. We probably should not expect exact agreement between the observed and predicted morphology, because the distribution of material at large distances, $r \gtrsim 2000$ AU, must depend as much on initial conditions—such as the shape of the cloud core—as on infall physics.

In addition to the near-IR colors and images, our models match the optical and near-IR spectral energy distributions (Fig. 14). Our best-fitting solution for 04016+2610 improves upon Paper I's results and reproduces the optical and near-IR fluxes very well. Although the envelope parameters for these two models are not identical, we can now fit the entire spectral energy distribution—0.55–100 μm—of a typical embedded source with the TSC density distribution if we allow a bipolar

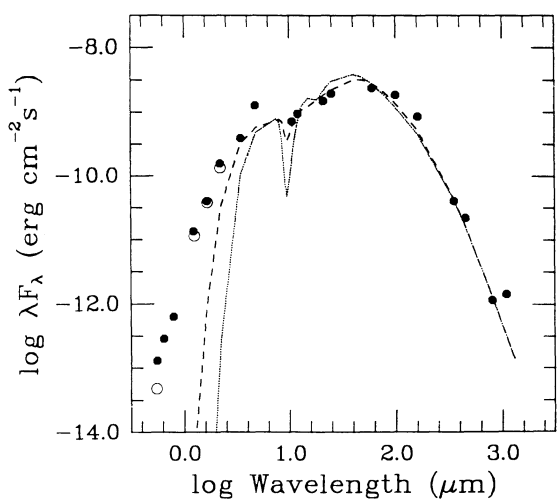

FIG. 14.—Comparison of observed and model spectral energy distributions for the embedded *IRAS* source 04016+2610. The filled circles represent the observed data, while the dashed and dotted lines plot one-dimensional models from Paper I. The open circles indicate predicted fluxes for the scattering models.

hole along the rotational axis. Aside from several objects described below, we find similarly good fits to the near-IR data for the rest of the embedded sample.

3.4. *Estimates for the Physical Properties of Individual Sources*

The near-IR colors and images of an embedded source obviously depend sensitively on *all* of the free parameters in TSC's infall solutions. The near-IR colors—$J-K$ and $H-K$—and the apparent extinction—$K-K_0$—vary considerably with $\dot{M}$ and R_c but do not change much for a wide variety of outflow geometries. In contrast, the size/shape of the outflow cavity constrains the appearance of the near-IR images. At present, we do not have enough information—such as the geometry of the molecular outflow and the polarization—to derive a best-fitting model for each source. However, we can define a *range* of infall models that account for the observed colors and $K-K_0$ and that also generally reproduce the observed morphology for each embedded source. By deriving $\dot{M}$, R_c, and i for a complete sample of embedded sources, we hope to minimize uncertainties in the average properties.

For each source, we compared the observed colors and $K-K_0$ to our results for the models listed in Table 6 to determine each combination of ($\dot{M}$, R_c, i) that reproduces the data. We then tried to eliminate some models by examining the images themselves to see if the size and morphology of the predicted images resemble the observations. In general, the broad-band images provide a poor discrimination between competing models. However, our three observable quantities—$J-K$, $H-K$, and $K-K_0$—still usually serve to constrain the three main physical variables in the infall model ($\dot{M}$, R_c, i). Table 4 summarizes our results. The scattering models do not place good limits on these variables for sources close to the reddening line in the color-color or color-extinction plane, because most infall models produce observables close to the reddening lines for some inclinations. In contrast to Paper I, we cannot derive a "best-fitting" model in the least-squares sense; we should be able to provide more stringent constraints on infall models once polarization data are available for the entire sample of embedded sources (see below).

In spite of these limitations, the scattering models suggest a relatively small dispersion in physical properties among the embedded sources in the Taurus-Auriga cloud (see Table 4). Several very blue objects require relatively low infall rates, $\sim$a few $\times 10^{-6}\ M_\odot\ \mathrm{yr}^{-1}$, compared to the rest of our sample. The relatively large $K-K_0$ estimated for 04248+2612, 04264+2433, 04302+2247, and 04368+2557 suggests an edge-on geometry with $i \gtrsim 60°$; the colors and $K-K_0$ for both 04295+2251 and 04489+3042 fall on the reddening line, so R_c and i are very uncertain. These two objects are the *only* embedded sources whose near-IR properties can be fit by infall models with large centrifugal radii, $R_c \gtrsim 300$ AU. The rest of our sample need higher infall rates, ~ 5–$10 \times 10^{-6}\ M_\odot\ \mathrm{yr}^{-1}$, and "standard" values for the centrifugal radius, $R_c \sim 50$–300 AU, to reproduce their very red $H-K$ and $J-K$ colors. Sources with $J-K \approx 4.5$–6 (04166+2706, 04169+2702, 04181+2655, 04181+2654A, and 04361+2547) require infall rates and centrifugal radii at the upper end of the standard ranges, while the lower values for $\dot{M}$ and R_c seem more applicable to the remaining sources. We infer higher inclinations for sources with larger $K-K_0$, so our results suggest $i \gtrsim 60°$ for most of the sample. The models suggest intermediate inclinations, $30° \lesssim i \lesssim 60°$, for 04181+2655, 04181+2654B, 04181+2654A, 04295+2251, and 04489+3042. None of our models suggest a pole-on geometry, $i \lesssim 30°$, for any embedded source. Paper I describes properties of individual sources in detail.

Although very few of the Taurus-Auriga embedded sources have measured polarization, observations of the three that do—04016+2610, GV Tau, and L1551 IRS5—confirm our parameter estimates. For example, Nagata et al. (1983) measured $P_K = 24\%$ and $P_H = 28\%$ for L1551 IRS5, with orientation almost perpendicular to the outflow axis, in an 8″ aperture. Tables 7 and 8 show that such large polarizations require nearly edge-on geometries for any infall rate (i.e., $\mu = 0.0$–0.5) and relatively small R_c ($\lesssim 100$ AU), in agreement with the actual geometry (see Nagata et al. 1983 and the discussion in Paper I). Tamura & Sato (1989) found $P_K = 2\%$–4% for GV Tau; if we assume that GV Tau B produces all of the polarization, then the light ratio of the two components at K suggests $P_K(\mathrm{GV\ Tau\ B}) \lesssim 14\%$–$28\%$ and $i \approx 60°$–$90°$. The near-IR colors and K extinction of GV Tau B similarly indicate large inclination, although the decomposition of the polarization between the two stars is admittedly very uncertain.

Our estimates for source parameters generally agree with those inferred in Paper I, which uses a least-squares technique to derive the best model fit to the 3–1000 μm spectral energy distribution. Both approaches require similar infall rates—$\dot{M} \sim 4 \times 10^{-6}\ M_\odot\ \mathrm{yr}^{-1}$—although our models tend to estimate *lower* infall rates than the radiative equilibrium models (Paper I) when the two approaches disagree (see below). This bias seems reasonable because more near-IR radiation can escape if the envelope has a lower opacity. The radiative equilibrium models probably provide a better estimate for the infall rate, because the peak of the spectral energy distribution depends most strongly on the density distribution and is not very sensitive to R_c and i. Our scattering models also generally indicate somewhat smaller values for R_c and larger source inclinations than do the radiative equilibrium models. These differences also appear reasonable, because the evacuated bipolar cavity included in the scattering model allows more near-IR radiation to escape the envelope. The radiative equilibrium models without holes can only increase the near-IR fluxes by increasing R_c and/or decreasing the inclination. Many objects clearly have bipolar flows and extended, asymmetric scattered light distributions, so our Monte Carlo models provide much better constraints on R_c and i. In spite of these potential problems, both approaches find a relatively small range in the centrifugal radius, $R_c \sim 10$–300 AU, for most sources.

We noted in Paper I that the TSC model can produce $R_c \lesssim 100$ AU during the estimated age of an embedded source, $\sim 10^5$ yr, for observed cloud rotation rates, $\Omega \lesssim 10^{13}\ \mathrm{s}^{-1}$ (e.g., Goodman et al. 1993). Interactions between a magnetic field and the cloud can also lead to flattened density distributions (e.g., Galli & Shu 1993a, b; Mouschovias & Morton 1991, 1992) and may be necessary for objects with apparent $R_c \sim 200$–300 AU.

We find large discrepancies between the results of Paper I and this work for only four sources: 04248+2612, 04302+2247, 04361+2547, and 04368+2557. Three of these objects—04248+2612, 04302+2247, and 04368+2557—possess large and very blue reflection nebulosity on near-IR images but are very red *IRAS* sources. Thus, we need a low

infall rate and high inclination to produce the near-IR colors, while Paper I's radiative equilibrium models require a higher infall rate to match the peak of the far-IR spectral energy distribution. Both approaches require a fairly large R_c to match the large near-IR images and the breadth of the energy distributions in each embedded source. We have difficulties reproducing the observed image sizes for these objects—especially 04368+2557—which might be caused by other complications, such as an embedded binary companion. The other object with a large disagreement, 04361+2547, also displays a bright near-IR nebula and is one of two sources—along with 04325+2402—whose nebula becomes redder with increasing aperture size. We estimate R_c = 200–300 AU for 04361+2547, while Paper I prefers R_c = 10 AU.

4. DISCUSSION

The observations presented in § 2 demonstrate that most embedded sources in the Taurus-Auriga cloud show extended near-IR emission on scales of 10″–20″, which corresponds to linear sizes of 1500–3000 AU at the distance of the cloud (see also Tamura et al. 1991). We find a large range in $J-K$ and $H-K$ colors for these class I sources. The bluest objects have colors similar to the reddest T Tauri stars in the cloud; redder objects lie slightly above the reddening line for standard ISM dust and have apparent K extinctions of 1–5 mag. The near-IR colors and nebular morphologies for this sample and the magnitude of linear polarization in several sources suggest scattered light produces most of the near-IR emission in these objects (see also Heyer et al. 1990).

The two-dimensional scattering models described in § 3 show that TSC's *physically plausible* infall solution can generally account for the near-IR observations. For reasonable dust grain parameters, we find that the large range in observed near-IR colors and apparent K extinctions *requires* envelopes with bipolar holes and *precludes* envelopes with large infall rates and centrifugal radii (e.g., $\dot{M} \lesssim 10^{-5}\ M_\odot\ \mathrm{yr}^{-1}$ and $R_c \lesssim$ 1000 AU). These results support the idea that *inflow and outflow occur simultaneously in deeply embedded, bipolar outflow sources* (e.g., Fig. 7*c* of Shu et al. 1987). Our average results for the infall rate and centrifugal radius—$\dot{M} \sim 4$–$5 \times 10^{-6}\ M_\odot\ \mathrm{yr}^{-1}$ and $R_c \sim 100$ AU—agree very well with Paper I's estimates and parameters expected for young stars having apparent ages of 1–3×10^{-5} yr (ALS; Myers et al. 1987; Kenyon et al. 1990). The scattering models also predict large polarization at near-IR wavelengths, and some sources—L1551 IRS5, 04016+2610, and perhaps GV Tau B—have observed polarizations comparable to those predicted by the models. Our models improve upon Paper I by predicting near-IR fluxes in good agreement with observations; thus we can now match observed spectral energy distributions from 1–1000 μm with a physical model for an infalling protostellar cloud.

In general, the observed sources appear slightly bluer at $J-K$ for a given $H-K$ than predicted by our calculations for the large R_c(>100 AU) models. The sizes of our model images are very sensitive to the shape of the cavity produced by a bipolar outflow and somewhat sensitive to the combination of the size of the centrifugal radius, R_c, and the infall rate $\dot{M}$. The observed near-IR colors and spectral energy distributions constrain R_c to be reasonably close to sizes typically estimated for disks surrounding T Tauri stars, ~100 AU (Adams et al. 1990; Beckwith et al. 1990; Keene & Masson 1990). However, we have no independent constraint on the shape (or the orientation) of the bipolar outflow in most of the embedded sources, so we have not tried to determine "best" hole shapes or orientations for individual objects.

Although ~10 embedded sources should have low inclinations, $i \lesssim 60°$, if they are oriented randomly in space, we find that at least 75% of the sample has $i \gtrsim 60°$. Our scattering models—together with Paper I's models—suggest that pole-on systems with low infall rates or very large R_c (or both) have near-IR colors and spectral energy distributions more similar to T Tauri stars with class II spectra than typical embedded stars with steeply rising spectra from 2–25 μm. Figure 5 shows that the near-IR colors of the bluest embedded sources overlap those of the reddest T Tauri stars (which include T Tau, DG Tau, and HL Tau among others). These very red T Tauri stars could be "almost embedded" sources, in the sense that they would be classified as true embedded (class I) sources if viewed at a larger inclination angle. Some of these objects have modest near-IR polarizations—$P_K \approx 2\%$–3% for DG Tau, FS Tau, and V892 Tau (Tamura & Sato 1989)—as predicted by the scattering models, while the rotational period and apparent rotational velocity in T Tau suggest it is viewed close to pole-on (e.g., Herbst et al. 1986). Systematic polarization measurements of very red TTS are needed to determine if these objects generally have polarizations between those of bluer TTS (which are essentially unpolarized) and the embedded sources. The orientation of the polarization vector can also discriminate between the large and small R_c models. The polarization in the 13″ aperture is oriented parallel to the outflow axis in most model images with $R_c > 200$ AU; in contrast, the polarization vectors lie perpendicular to the evacuated cavity for small R_c models.

Previous extinction studies have shown that the near-IR extinction curve appears universal in dense molecular clouds (e.g., Martin & Whittet 1990) and in more diffuse clouds where the optical and ultraviolet (UV) extinction vary considerably from one line-of-sight to the next (Jones & Hyland 1980; Smith 1987; Cardelli, Clayton, & Mathis 1989). These studies suggest the properties of the large grains—with radii exceeding 0.1 μm—that produce the near-IR extinction do not change much from cloud to cloud, even though the smaller grains responsible for the UV extinction do vary considerably. Our results provide further evidence that the properties of the larger grains remain roughly independent of the local cloud density, because the scattering models provide the best agreement with near-IR observations for "standard" grain properties (the MRN distribution). In particular, we find that the larger PTW grains produce too much near-IR extinction and too little near-IR polarization for the embedded sources in our sample.

Although standard grain properties produce the correct amount of *relative* extinction as a function of wavelength for the embedded sources, our model images of extended near-IR emission are not as large at K as many of the Taurus-Auriga objects. Sellgren, Werner, & Dinerstein (1992) derived a similar result for dust in reflection nebulae. Their standard grain models also fit the colors of the scattered light in these sources, but they failed to reproduce the large K surface brightness of the observed images. Sellgren et al. (1992) suggested that increasing the K albedo beyond that indicated by Draine & Lee's (1984) predictions would produce brighter model images, and this change would also bring our model images into better

agreement with observations. However, our models produce reasonable K extinctions and polarizations in addition to the near-IR colors, so any change in the K albedo that increases the K surface brightness of the scattered light nebula must not modify these observables significantly.

We suggested above that changes in the standard source geometry—such as the shape and dust content of the bipolar cavity—represent another promising way to construct model images closer to those observed. However, any additional scattering calculations have few observational constraints besides the morphology of the near-IR images. Aside from L1551 IRS5, the molecular outflows in the Taurus-Auriga embedded sources have not been mapped with sufficient spatial resolution to determine the inclination and size of the outflow cavity, and few sources have high enough quality optical images to place additional limits on the grain properties. Once these data exist, new scattering calculations will be able to provide more stringent tests of the standard infall model for the formation of low-mass stars.

We acknowledge the KPNO staff for assistance with the observations reported in this paper. We also thank M. Barsony, N. Calvet, and E. Lada for useful comments throughout this project, and the referee, F. Shu, for suggestions that improved our presentation. This research was supported by the Scholarly Studies and Predoctoral Fellowship Programs of the Smithsonian Institution and the National Aeronautics and Space Administration through grant NAGW-2919. Kitt Peak National Observatory is operated by the National Optical Astronomy Observatory under contract to the National Science Foundation. IRAF is distributed by the National Optical Astronomy Observatories, which is operated by the Association of Universities for Research in Astronomy, Inc., under contract to the National Science Foundation.

REFERENCES

Adams, F. C., Emerson, J. P., & Fuller, G. A. 1990, ApJ, 357, 606
Adams, F. C., Lada, C. J., & Shu, F. H. 1987, ApJ, 312, 788 (ALS)
Adams, F. C., & Shu, F. H. 1986, ApJ, 308, 836
Barsony, M., & Kenyon, S. J. 1992, ApJ, 384, L53
Bastien, P., & Ménard, F. 1988, ApJ, 326, 334
———. 1990, ApJ, 364, 232
Beckwith, S. V. W., Sargent, A. I., Chini, R., & Güsten, R. 1990, AJ, 99, 924
Beichman, C. A., Boulanger, F., & Moshir, M. 1992, ApJ, 386, 248
Beichman, C. A., Myers, P. C., Emerson, J. P., Harris, S., Mathieu, R., Benson, P. J., & Jennings, R. E. 1986, ApJ, 307, 337
Benson, P. J., & Myers, P. C. 1989, ApJS, 71, 89
Butner, H. M., Evans, N. J. II, Lester, D. F., Levreault, R. M., & Strom, S. E. 1991, ApJ, 376, 636
Cardelli, J. A., Clayton, G. C., & Mathis, J. S. 1989, ApJ, 345, 245
Cassen, P., & Moosman, A. 1981, Icarus, 48, 353
Draine, B., & Lee, H. M. 1984, ApJ, 285, 89
Elias, J. H., Frogel, J. A., Matthews, K., & Neugebauer, G. 1982, AJ, 87, 1029
Ellis, T., et al. 1992, Proc. SPIE, in press
Fowler, A. M., et al. 1987, Opt. Engineering, 26, 232
Galli, D., & Shu, F. H. 1993a, ApJ, in press
———. 1993b, ApJ, in press
Goodman, A. A., Benson, P. J., Fuller, G. A., & Myers, P. C. 1993, ApJ, 406, 528
Gomez, M., Jones, B. F., Hartmann, L., Kenyon, S. J., Stauffer, J. R., Hewett, R., & Reid, I. N. 1992, AJ, 104, 762
Herbst, W., Booth, J. F., Chugainov, P. F., Zajtseva, G. V., Barksdale, W., Terranegra, L., & Vrba, F. J. 1986, ApJ, 310, L71
Heyer, M. H., Ladd, E. F., Myers, P. C., & Campbell, B. 1990, AJ, 99, 1585
Heyer, M. H., Snell, R. L., Goldsmith, P. F., & Myers, P. C. 1987, ApJ, 321, 370
Keene, J., & Masson, C. R. 1990, ApJ, 355, 635
Kenyon, S. J., Calvet, N., & Hartmann, L. 1993, ApJ, 414, 676 (Paper I)
Kenyon, S. J., & Hartmann, L. 1990, ApJ, 349, 197
———. 1993, in preparation
Kenyon, S. J., Hartmann, L. W., Strom, K. M., & Strom, S. E. 1990, AJ, 99, 869
Königl, A. 1991, ApJ, 370, L39
Jones, T. J., & Hyland, A. R. 1980, MNRAS, 192, 359
Leinert, Ch., & Haas, M. 1989, A&A, 222, 110
Martin, P. G., & Whitett, D. C. B. 1990, ApJ, 357, 113
Mathis, J. S. 1990, ARA&A, 28, 37
Mathis, J. S., Rumpl, W., & Nordsieck, K. H. 1977, ApJ, 217, 425 (MRN)
Mazzitelli, I. 1989, in ESO Conf. and Wksp. Proc. No. 33, Low-Mass Star Formation and Pre–Main-Sequence Objects, ed. B. Reipurth (Noordwijk: ESO), 433
Moriarty-Schieven, G. H., Wannier, P. G., Tamura, M., & Keene, J. B. 1992, ApJ, 400, 260
Mouschovias, T. Ch., & Morton, S. A. 1991, ApJ, 371, 296
———. 1992, ApJ, 390, 166
Myers, P. C., Fuller, G. A., Mathieu, R. D., Beichman, C. A., Benson, P. J., Schild, R. E., & Emerson, J. P. 1987, ApJ, 319, 340
Myers, P. C., Heyer, M., Snell, R. L., & Goldsmith, P. F. 1988, ApJ, 324, 907
Nagata, T., Sato, S., & Kobayashi, Y. 1983, A&A, 119, L1
Pendleton, Y., Tielens, A. G. M., & Werner, M. W. 1990, ApJ, 349, 107 (PTW)
Pudritz, R. E., & Norman, C. A. 1986, ApJ, 301, 571
Savage, B. D., & Mathis, J. S. 1979, ARA&A, 17, 73
Sellgren, K., Werner, M. W., & Dinerstein, H. L. 1992, ApJ, 400, 238
Shu, F. H. 1977, ApJ, 214, 488
Shu, F. H., Adams, F. C., & Lizano, S. 1987, ARA&A, 25, 23
Shu, F. H., Lizano, S., Ruden, S. P., & Najita, J. 1988, ApJ, 328, L19
Smith, R. G. 1987, MNRAS, 227, 943
Stahler, S. W. 1983, ApJ, 274, 822
———. 1988, ApJ, 332, 804
Tamura, M., Gatley, I., Waller, W., & Werner, M. W. 1991, ApJ, 374, L25
Tamura, M., & Sato, S. 1989, AJ, 98, 1368
Terebey, S., Beichman, C. A., Gautier, T. N., & Hester, J. J. 1990, ApJ, 362, L63
Terebey, S., Shu, F. H., & Cassen, P. 1984, ApJ, 286, 529 (TSC)
Terebey, S., Vogel, S. N., & Myers, P. C. 1989, ApJ, 340, 472
Ulrich, R. K. 1976, ApJ, 210, 377
White, R. L. 1979, ApJ, 229, 954
Whitney, B. A., & Hartmann, L. 1992, ApJ, 395, 529
———. 1993, ApJ, 402, 605
Wilking, B. A., Lada, C. J., & Young, E. T. 1989, ApJ, 340, 823